Article

Cancer Cell

ATRX In-Frame Fusion Neuroblastoma Is Sensitive to EZH2 Inhibition via Modulation of Neuronal Gene Signatures

Graphical Abstract

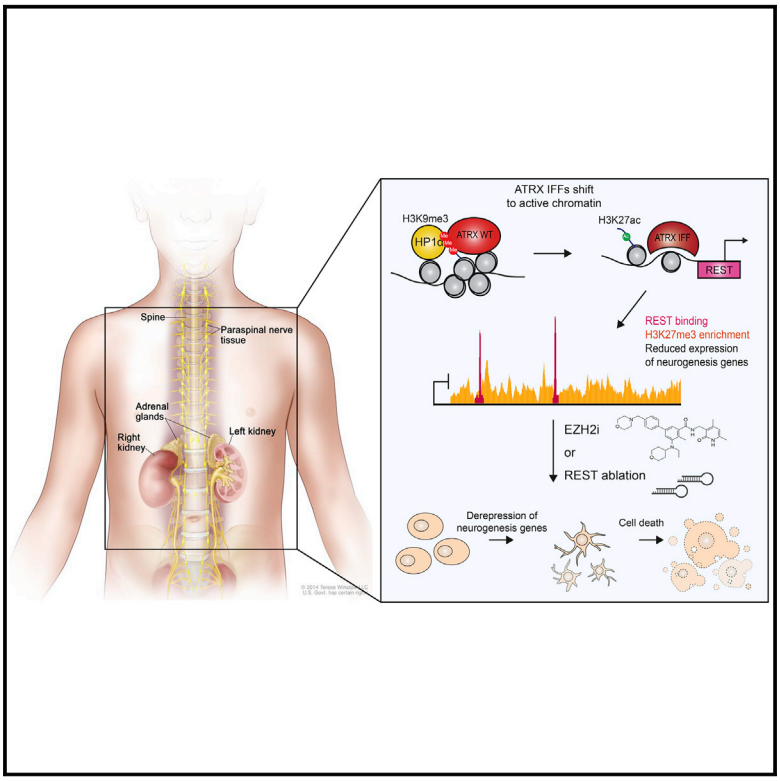

Highlights

- ATRX IFFs are redistributed genome wide and are enriched at active promoters
- The neuronal silencing transcription factor *REST* is an ATRX IFF target gene
- REST and EZH2 silence neuronal gene programs in ATRX IFF NB
- REST loss or EZH2 inhibition induces neuronal gene expression programs and NB cell death

Authors

Zulekha A. Qadeer, David Valle-Garcia, Dan Hasson, ..., Miguel F. Segura, Michael A. Dyer, Emily Bernstein

Correspondence

emily.bernstein@mssm.edu

In Brief

Qadeer et al. show that ATRX in-frame fusions (IFF), found in a subset of neuroblastomas, are redistributed from wild-type ATRX-binding sites to other genomic regions, including the *REST* promoter. REST expression silences neuronal differentiation genes, which can be derepressed with EZH2 inhibitors to suppress ATRX IFF cell growth.

Qadeer et al., 2019, Cancer Cell *36*, 512–527
November 11, 2019
https://doi.org/10.1016/j.ccell.2019.09.002

CellPress

CellPress

Cancer Cell
Article

ATRX In-Frame Fusion Neuroblastoma Is Sensitive to EZH2 Inhibition via Modulation of Neuronal Gene Signatures

Zulekha A. Qadeer,[1,2,5] David Valle-Garcia,[1,14,16] Dan Hasson,[1,16] Zhen Sun,[1,2,15] April Cook,[1] Christie Nguyen,[1,2] Aroa Soriano,[6] Anqi Ma,[1,3] Lyra M. Griffiths,[7,16] Maged Zeineldin,[7,16] Dan Filipescu,[1] Luz Jubierre,[6] Asif Chowdhury,[1] Orla Deevy,[1] Xiang Chen,[8] David B. Finkelstein,[8] Armita Bahrami,[9] Elizabeth Stewart,[7,10] Sara Federico,[10] Soledad Gallego,[11] Fumiko Dekio,[4] Mary Fowkes,[4] David Meni,[12] John M. Maris,[13] William A. Weiss,[5] Stephen S. Roberts,[12] Nai-Kong V. Cheung,[12] Jian Jin,[1,2,3] Miguel F. Segura,[6] Michael A. Dyer,[7] and Emily Bernstein[1,2,17,*]

[1]Department of Oncological Sciences, Icahn School of Medicine at Mount Sinai, New York, NY 10029, USA
[2]Graduate School of Biomedical Sciences, Icahn School of Medicine at Mount Sinai, New York, NY 10029, USA
[3]Department of Pharmacological Sciences, Icahn School of Medicine at Mount Sinai, New York, NY 10029, USA
[4]Department of Pathology, Icahn School of Medicine at Mount Sinai, New York, NY 10029, USA
[5]Departments of Neurology, Neurosurgery, and Pediatrics, University of California, San Francisco, San Francisco, CA 94158, USA
[6]Laboratory of Translational Research in Child and Adolescent Cancer, Vall d'Hebron Institut de Recerca (VHIR), Barcelona 08035, Spain
[7]Department of Developmental Neurobiology, St. Jude Children's Research Hospital, Memphis, TN 38105, USA
[8]Department of Computational Biology, St. Jude Children's Research Hospital, Memphis, TN 38105, USA
[9]Department of Pathology, St. Jude Children's Research Hospital, Memphis, TN 38105, USA
[10]Department of Oncology, St. Jude Children's Research Hospital, Memphis, TN 38105, USA
[11]Pediatric Oncology and Hematology Department, University Hospital Vall d'Hebron, Barcelona 08035, Spain
[12]Department of Pediatrics, Memorial Sloan Kettering Cancer Center, New York, NY 10065, USA
[13]Center for Childhood Cancer Research at the Children's Hospital of Philadelphia, Perlman School of Medicine at the University of Pennsylvania, Philadelphia, PA 19104, USA
[14]Present address: Department of Cell Biology, Harvard Medical School, Boston, MA 02115, USA
[15]Present address: Cell Biology Program and Center for Epigenetics Research, Memorial Sloan Kettering Cancer Center, New York, NY 10065, USA
[16]These authors contributed equally
[17]Lead Contact
*Correspondence: emily.bernstein@mssm.edu
https://doi.org/10.1016/j.ccell.2019.09.002

SUMMARY

ATRX alterations occur at high frequency in neuroblastoma of adolescents and young adults. Particularly intriguing are the large N-terminal deletions of ATRX (Alpha Thalassemia/Mental Retardation, X-linked) that generate in-frame fusion (IFF) proteins devoid of key chromatin interaction domains, while retaining the SWI/SNF-like helicase region. We demonstrate that ATRX IFF proteins are redistributed from H3K9me3-enriched chromatin to promoters of active genes and identify *REST* as an ATRX IFF target whose activation promotes silencing of neuronal differentiation genes. We further show that ATRX IFF cells display sensitivity to EZH2 inhibitors, due to derepression of neurogenesis genes, including a subset of REST targets. Taken together, we demonstrate that ATRX structural alterations are not loss-of-function and put forward EZH2 inhibitors as a potential therapy for ATRX IFF neuroblastoma.

Significance

ATRX (Alpha Thalassemia/Mental Retardation, X-linked) is an epigenetic regulator mutated in pediatric and adult tumors. However, the consequences of *ATRX* alterations in cancer and on the epigenome remain ill defined. Focusing on the large structural variations of *ATRX* in neuroblastoma, we find that the consequent in-frame fusion (IFF) proteins lacking key chromatin-binding modules are altered in their genomic binding. ATRX IFFs localize to active promoters, notably that of *REST*, which encodes a neuronal transcriptional repressor. REST depletion and inhibition of EZH2 promote derepression of neuronal genes and cell death, suggesting cooperative pathways for silencing neuronal differentiation in ATRX IFF neuroblastoma. These studies support the therapeutic targeting of ATRX IFF neuroblastoma with EZH2 inhibitors and reveal REST as a key player in this aggressive neuroblastoma subtype.

INTRODUCTION

Neuroblastoma (NB) is one of the most common and aggressive pediatric nervous system tumors with poor overall survival, particularly for older children (Cheung and Dyer, 2013; Dyer et al., 2017). NB is thought to arise from impaired differentiation of progenitor cells of the peripheral nervous system (Brodeur, 2003). Prognosis of patients is associated with age at diagnosis, with spontaneous regression observed in early childhood (Cheung and Dyer, 2013; Mossé et al., 2014). In contrast, indolent or chronic NB in adolescents and young adults is characterized by protracted disease progression and marked by the absence of *MYCN* amplifications. *ATRX* alterations are the most common recurring event in this indolent clinical subtype (~30%) (Cheung et al., 2012; Dyer et al., 2017; Molenaar et al., 2012), which is associated with overall poor survival and lacks effective therapies (Cheung et al., 2012). Besides point mutations and indels identified at the *ATRX* locus, studies in NB have identified large deletions near the 5′ coding region of *ATRX* leading to in-frame fusion (IFF) protein products of unknown significance.

ATRX (Alpha Thalassemia/Mental Retardation, X-linked) is an SWI/SNF-like chromatin remodeler with diverse roles in chromatin regulation. The ATRX protein contains multiple highly conserved domains, including an N-terminal ADD (ATRX-DNMT3-DNMT3L) domain that binds trimethylated histone H3 at lysine 9 (H3K9me3) when unmethylated at H3K4 (Dhayalan et al., 2011; Eustermann et al., 2011; Iwase et al., 2011), an HP1α-binding motif (Le Douarin et al., 1996; Lechner et al., 2005), and a putative EZH2 interaction domain identified through a yeast two-hybrid screen (Cardoso et al., 1998). In addition, ATRX interacts with DAXX to deposit H3.3 at heterochromatic regions (e.g., telomeres and repetitive DNA) (Drané et al., 2010; Goldberg et al., 2010; Wong, 2010). ATRX has also been shown to negatively regulate macroH2A deposition at telomeres and the α-globin genes cluster in erythroid cells (Ratnakumar et al., 2012). Finally, ATRX has an SWI/SNF-like helicase domain, responsible for mediating DNA accessibility (reviewed in Dyer et al., 2017; Ratnakumar and Bernstein, 2013). Notably, ATRX IFFs identified in NB lack the majority of these chromatin-binding modules with the exception of the C-terminal ATP-dependent helicase domain.

REST (RE-1 Silencing Transcription Factor), also known as neuron-restrictive silencer factor (NRSF), is a transcriptional repressor that binds DNA in a sequence-specific manner at neuron-restrictive silencer elements known as RE1 motifs (Chong et al., 1995; Schoenherr and Anderson, 1995). The primary function of REST is to suppress neuronal gene transcription in non-neuronal cells. REST plays a key role in neuronal development, with *REST* expression declining as neural progenitors progress to terminal neurons (Ballas and Mandel, 2005). Genome mapping of REST suggests that its intricate function in regulating gene expression depends on co-factors including SIN3A, the CoREST complex, Polycomb Repressive Complex 1 (PRC1), and PRC2 (Dietrich et al., 2012; McGann et al., 2014; Rockowitz et al., 2014). *REST* is overexpressed in several aggressive tumors of the nervous system, including neuroblastoma (stage 4 *MYCN* non-amplified) (Liang et al., 2014), medulloblastoma, and glioblastoma (Dobson et al., 2019; Taylor et al., 2012; Zhang et al., 2016).

We hypothesized that ATRX IFFs, which lack several key chromatin interaction domains, contribute to aggressive NB via reorganization of the chromatin landscape and, in turn, transcriptional deregulation. In this study, we aimed to decipher the underlying biology of ATRX IFFs in NB, a tumor for which effective therapeutic strategies remain obscure, and exploit identified epigenetic dependencies.

RESULTS

Identification and Characterization of NB Cells Harboring ATRX IFFs

To explore the role of *ATRX* alterations in NB, we screened an extensive panel of patient-derived cell lines, patient-derived xenograft (PDX) models, and human tumor samples to identify ATRX IFFs. Utilizing PCR-based assays that favor amplification of an ATRX IFF gene product versus full-length ATRX from a total cDNA pool (Cheung et al., 2012; Qadeer et al., 2014), we identified two human-derived NB cell lines, SK-N-MM and CHLA-90, which carry distinct structural variations in the *ATRX* gene (Cheung et al., 2012; Molenaar et al., 2012) (Figures 1A, S1A, and S1B). *ATRX* is located on the X chromosome, thus the male cell line CHLA-90 carries a single *ATRX* copy harboring an IFF (exons 2 to 10). The female cell line SK-N-MM harbors *ATRX* alterations on both alleles: an ATRX IFF (exons 1 to 11) and a nonsense mutation (K1367X) (Cheung et al., 2012) (Figures 1A, S1C, and S1D). We characterized these two ATRX IFF cell lines derived from stage 4 NB along with LAN-6 and SK-N-FI (*ATRX* wild-type [WT]; stage- and age-matched; *MYCN* non-amplified NB lines) for mutations and copy-number variations, as well as telomere status. We found that ATRX IFF NB cell lines displayed long telomeres and low levels of the telomerase reverse transcriptase mRNA (Figure S1E) indicative of alternative lengthening of telomeres (ALT), lacked *MYCN* amplifications (Figures S1F and S1G), and harbored few recurrent mutations (Table S1), all consistent with clinical reports (Cheung and Dyer, 2013; Dyer et al., 2017).

ATRX IFFs Are Chromatin Bound and Reside in Complexes Distinct from WT ATRX

Using an antibody against the C terminus of ATRX that recognizes both WT and IFF forms of ATRX, we detected full-length ATRX protein in whole-cell extracts at 280 kDa in LAN-6 and SK-N-FI and ATRX IFF protein products at ~150–170 kDa in SK-N-MM and CHLA-90, respectively (Figures S2A and S2B). Although ATRX IFFs lack key protein interaction domains (Figure 1A), they remain chromatin bound, albeit at reduced levels compared with WT NB cell lines LAN-6 and SK-N-FI (Figure 1B). We additionally observed that while WT cell lines displayed ATRX localization in heterochromatin foci marked by HP1α and its cognate modification H3K9me3, ATRX IFF cells exhibited loss of ATRX- and HP1α-enriched foci (Figure 1C), although H3K9me3 was largely unaffected (Figure S2C). This is in line with previous reports demonstrating cooperation between the ADD domain of ATRX and HP1 in chromatin recruitment to H3K9me3-decorated chromatin (Eustermann et al., 2011; Iwase et al., 2011; Kovatcheva et al., 2017). The diffuse nuclear distribution of ATRX away from H3K9me3-containing heterochromatin is consistent with the finding that ATRX IFF protein displayed increased sensitivity to salt extraction compared with WT ATRX (Figures 1D and S2D). Collectively, we find ATRX IFFs to be altered in their nuclear localization and less stably bound to

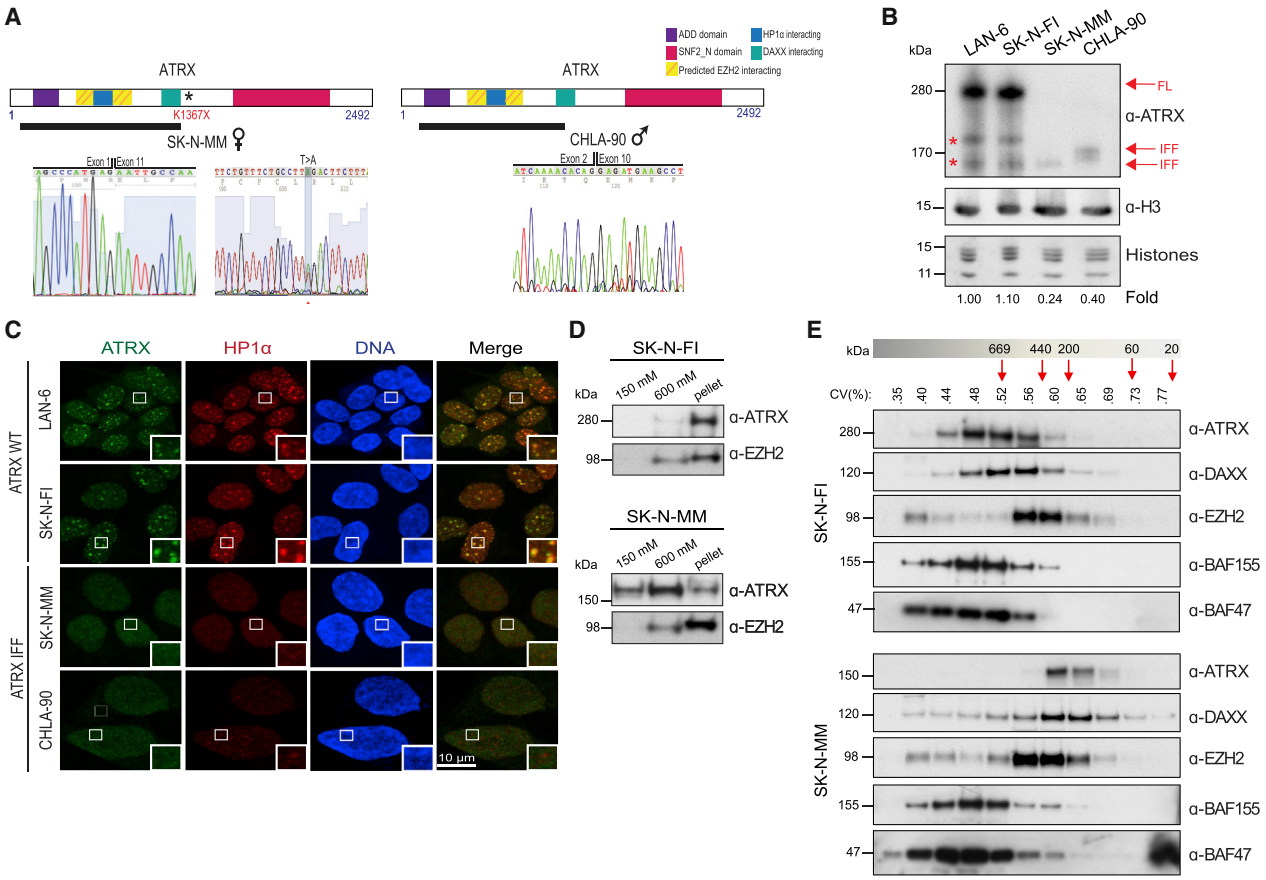

Figure 1. ATRX IFF Proteins Are Chromatin Bound and in Complexes Distinct from WT ATRX

(A) Schematic of ATRX protein product with domains depicted and alterations identified in SK-N-MM and CHLA-90. Black bar underneath indicates N-terminal deletion of IFFs. Sanger sequencing traces from SK-N-MM and CHLA-90 cDNA identifying *ATRX* alterations.

(B) Immunoblot for ATRX demonstrating ATRX IFF protein products in the extracted chromatin fraction, indicated by red arrows. Asterisks denote putative ATRX isoforms. H3 and amido black staining of histones used as loading controls. Protein fold change measured relative to total H3.

(C) Immunofluorescence for ATRX and HP1α in NB cells. Scale bar, 10 μm.

(D) Immunoblots of ATRX and EZH2 in cellular fractions extracted at indicated salt concentrations from nuclei of NB cells. Pellet represents insoluble material from 600 mM NaCl extraction.

(E) Size-exclusion chromatography fractions probed for endogenous ATRX, DAXX, and EZH2 in ATRX WT and IFF NB cell lines. BAF155 and BAF47 (BAF complex subunits) used as reference for large chromatin complexes. CV, column volume.

See also Figures S1 and S2; Table S1.

chromatin than WT ATRX, which may consequently play a role in deregulating chromatin states.

Size-exclusion chromatography of endogenous ATRX-containing complexes in SK-N-FI (ATRX WT) and SK-N-MM (ATRX IFF) cells suggested that these proteins were in distinct complexes. ATRX IFF protein appeared in a smaller complex of ~300 kDa compared with that of WT ATRX (~700 kDa), which is a greater size difference than expected simply due to the IFF deletion (~100 kDa) (Figure 1E). In both scenarios, ATRX co-fractionated with DAXX, although the deletion in SK-N-MM removes a large portion of the DAXX-binding domain; however, neither co-fractionated with EZH2 (Figure 1E). We next investigated ATRX interactions with key chromatin-binding partners by immunoprecipitation (IP), again using the antibody that recognizes the C terminus of ATRX (Figure S2A). As anticipated, DAXX binding was largely abrogated in SK-N-MM, but not CHLA-90 (Figure S2E), whose IFF retains the DAXX-binding domain (Figure 1A). Together with clinical reports of some ATRX IFFs preserving this domain (Cheung et al., 2012; Molenaar et al., 2012), these data suggest that loss of the ATRX-DAXX interaction may not be critical for driving disease. Because of the reported interaction with EZH2 (Cardoso et al., 1998; Sarma et al., 2014), we probed ATRX IPs for EZH2. Despite similar levels of EZH2 across WT and ATRX IFF NB lines, we failed to detect an interaction with ATRX (Figures S2E and S2F). We were also unable to detect an ATRX-EZH2 interaction by reverse co-immunoprecipitation experiments with EZH2 in NB cells (Figure S2G). This suggests that ATRX-EZH2 interactions may be context dependent or mediated by additional unknown factors.

ATRX IFFs Redistribute from H3K9me3-Enriched Regions to Active Promoters

Based on the altered nuclear localization pattern and changes in complex formation of ATRX IFFs, we performed chromatin

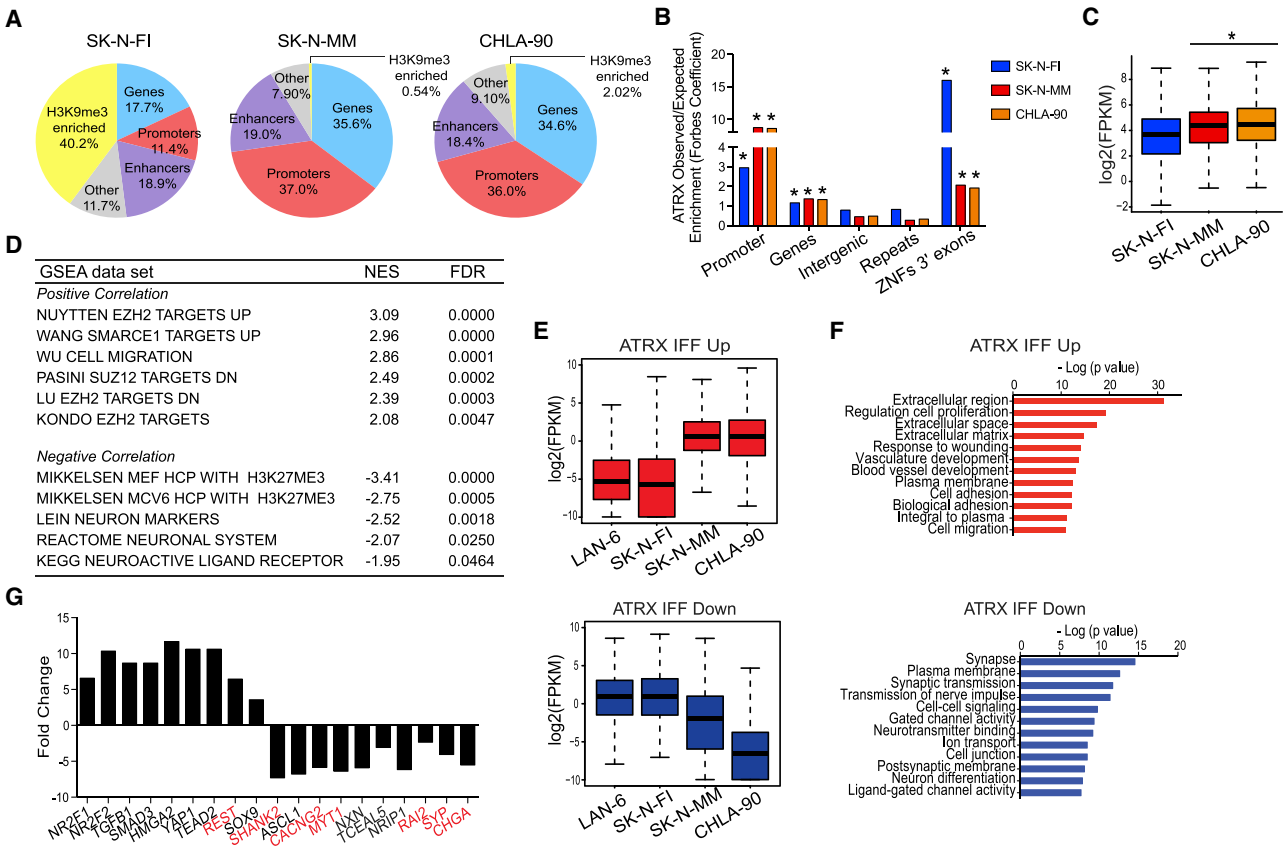

Figure 2. ATRX IFF Proteins Redistribute from H3K9me3-Enriched Regions to Promoters of Actively Expressed Genes

(A) Pie chart displaying the percentage of ATRX peaks occupying promoters, enhancers, gene bodies, H3K9me3-enriched, and other regions for each cell line. Promoters: transcriptional start site (TSS) ±2 kb; gene bodies: TSS to transcriptional end site (TES); enhancers: called based on H3K27ac levels and overlapped with ATRX peaks; H3K9me3 enriched: ATRX peaks overlapped with H3K9me3 peaks; all other regions defined as "other."

(B) Observed over expected random distribution of significant ATRX peaks in chromatin state categories in ATRX WT and IFF cells for each ChIP. Statistical significance assessed using hypergeometric test. *$p < 0.05$.

(C) Box plots of mRNA expression levels from SK-N-FI, SK-N-MM, and CHLA-90 at ATRX IFF-bound promoters (n = 788). Statistical significance assessed using Student's unpaired t test comparing each ATRX IFF cell line with SK-N-FI. Box plots represent the 25th and 75th percentiles, black line indicates median, and whiskers represent extremes. *$p < 0.05$.

(D) Summary of gene set enrichment analysis (GSEA) terms associated with differentially expressed genes in ATRX IFF cells.

(E) Box plots of expression levels of differential genes upregulated (n = 1,400) and downregulated (n = 826) in ATRX IFF NB cells. Box plots represent the 25th and 75th percentiles, black line indicates median, and whiskers represent extremes. Statistical significance assessed using one-way ANOVA.

(F) Gene ontology (GO) analysis of ATRX IFF Up and ATRX IFF Down genes. Enriched terms ranked by most significant p value.

(G) Expression levels of representative genes upregulated in RNA-seq. Fold change plotted, mean $\log_2$ (fragments per kilobase of transcript per million [FPKM]) of ATRX IFF cells over mean $\log_2$ (FPKM) of ATRX WT cells. REST and its target genes identified by ChIP-seq enrichment analysis (ChEA, Chen et al., 2013a) and Harmonizome (Rouillard et al., 2016) labeled in red.

See also Figure S3 and Table S2.

immunoprecipitation sequencing (ChIP-seq) using the C-terminal ATRX antibody that recognizes both WT ATRX (SK-N-FI) and IFFs (SK-N-MM and CHLA-90) (Figures S2A and S2B). We also mapped relevant histone modifications, including H3K9me3, to which the ADD domain binds (Figure S3A). We observed a significant enrichment of WT ATRX peaks ("ATRX WT-bound") at H3K9me3-enriched chromatin, composed of genes, intergenic regions, and the 3′ exons of ZNF genes as we previously reported (Valle-García et al., 2016); however, such ATRX IFF enrichment was strikingly lacking in ATRX IFF NB cells (Figures 2A, 2B, S3B, and S3C; Table S2). This differential distribution of ATRX IFFs was present despite the fact that H3K9me3 distribution was not altered genome wide (Figure S3A and Table S2). In stark contrast, ATRX IFF proteins significantly occupied more promoters and gene bodies ("ATRX IFF-bound") than WT ATRX (Figures 2A, 2B, and S3D; Table S2). Promoters with the highest ATRX IFF enrichment compared with WT (fold change ≥3.05, n = 788; Figure S3E) harbored higher levels of H3K27ac, indicative of active transcription (Figures S3E and S3F). Together, these data suggest that while ATRX IFFs retain the ability to bind to chromatin, they are depleted from H3K9me3-enriched chromatin, and are instead localized at active genes and promoters compared with WT ATRX.

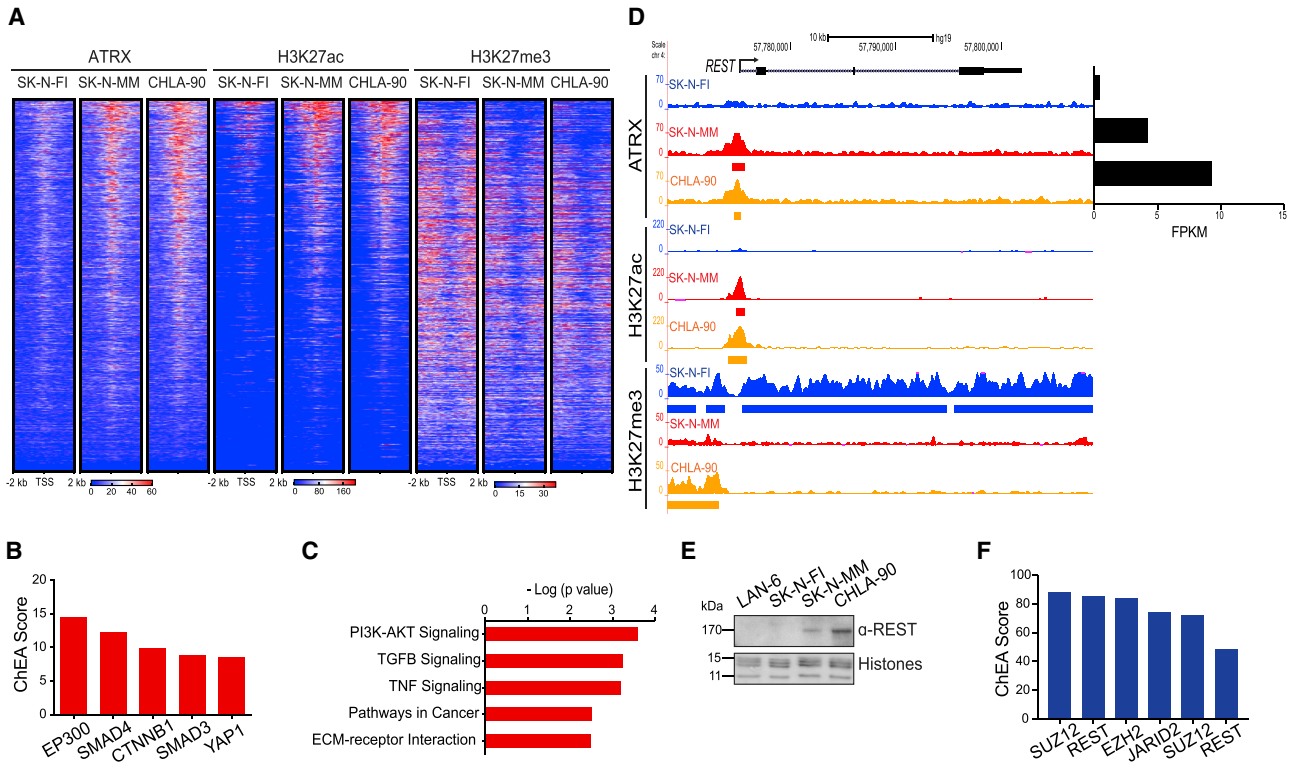

Figure 3. ATRX IFF Proteins Are Associated with Active Transcription and REST Expression

(A) Heatmap of ATRX, H3K27ac and H3K27me3 enrichment in the promoters of ATRX IFF Up genes (promoters: TSS ±2 kb).

(B) Transcription factors associated with ATRX IFF bound/IFF Up genes (n = 346) as identified by ChEA, ranked based on ChEA combined score.

(C) KEGG pathway analysis of ATRX IFF bound/IFF Up genes. Enriched terms ranked by most significant p value.

(D) UCSC Genome Browser snapshot of ATRX, H3K27ac, and H3K27me3 ChIP-seq at the *REST* locus (y axis = reads per kilobase per million reads). Bar graph (right) indicates expression values (FPKM) for REST in corresponding cells. Significant peaks called by MACS2 and SICER are annotated under each profile by colored bars (false discovery rate [FDR] = 5×10^{-2} for SK-N-FI, 5×10^{-3} for SK-N-MM, 5×10^{-4} for CHLA-90 ATRX peaks; and 1×10^{-5} for all H3K27ac and H3K27me3 peaks).

(E) Immunoblot of REST in the extracted chromatin fraction of NB cells. Amido black staining of histones used as loading control.

(F) ChEA of ATRX IFF Down genes (n = 826), ranked by ChEA combined score.

See also Figure S3 and Table S3.

ATRX IFF NB Exhibits a Suppressed Neuronal Differentiation Program

Transcriptome analysis of LAN-6, SK-N-FI, SK-N-MM, and CHLA-90 cells revealed that ATRX IFF NB cell lines harbored a unique transcriptional program relative to ATRX WT cells (Figure S3G). Notably, ATRX IFF-bound genes displayed higher levels of expression in ATRX IFF cells compared with ATRX WT cells (Figure 2C), corroborating that ATRX IFF proteins are indeed bound at transcriptionally active regions. Differentially expressed genes (fold change ≥ 8; Figure S3G) in ATRX IFF cells displayed a positive correlation with PRC2 targets and anti-correlation with neuronal markers (Figure 2D and Table S2). We next focused on the shared 1,400 upregulated "ATRX IFF Up" and 826 downregulated "ATRX IFF Down" genes (Figures 2E and S3G; Table S2). Gene ontology (GO) (Huang et al., 2009) analysis demonstrated that ATRX IFF Up genes are involved in proliferation, adhesion, and migration, while ATRX IFF Down genes are implicated in synaptic functions and neuronal differentiation (Figure 2F and Table S2). These differentially expressed genes, including *NR2F1*, *YAP1*, *REST* (ATRX IFF Up), and *NXN* (ATRX IFF Down) (Figure 2G), were validated at both the mRNA and protein level (Figures S3H and S3I). Furthermore, consistent with gene set enrichment analysis and GO analysis, ATRX IFF NB cells presented a more migratory phenotype than WT cells (Figure S3J).

Integration of RNA-sequencing (RNA-seq) and ChIP-seq data revealed that ATRX IFF Up genes were enriched for ATRX IFF binding and H3K27ac, with reduced H3K27me3 levels (Figure 3A). We next focused on the "ATRX IFF-bound/ATRX IFF Up" genes (n = 346) (Table S3). Using ChIP-seq enrichment analysis (ChEA), a tool that correlates gene signatures with ChIP-seq datasets (Chen et al., 2013a), we found ATRX IFF-bound/ATRX IFF Up genes as reported targets of the H3K27 acetyltransferase P300 and the transforming growth factor β (TGFβ) pathway (Figures 3B and 3C; Table S3). The TGFβ pathway is overexpressed in cancer (Massagué, 2012) and is an important modulator of neuroectoderm development (Jia et al., 2009). Furthermore, ATRX IFF NB cells were dependent on expression of ATRX IFF, as knockdown with short hairpin RNAs (shRNAs) targeting the retained C-terminal region of ATRX led to a significant proliferative arrest in both SK-N-MM and CHLA-90 (Figures S3K and S3L). This suggests an essential role of ATRX IFFs in maintaining

the viability of ATRX IFF NB cells through maintenance of these pathways.

Notable among the ATRX IFF-bound/IFF Up genes was *REST*, which encodes a transcriptional repressor that mediates the silencing of neuronal genes by recruiting co-repressor complexes. Both SK-N-MM and CHLA-90 displayed peaks of ATRX IFF and H3K27ac at the *REST* promoter, and were devoid of H3K27me3 across the gene body (Figure 3D). Moreover, the REST protein could be detected in both ATRX IFF lines (Figure 3E). Consistent with *REST* expression in ATRX IFF NB cells, REST target genes predicted by ChEA were represented among the ATRX IFF Down genes (Figure 2G) and ChEA-implicated ATRX IFF Down genes as enriched for REST and PRC2 complex members (Figure 3F).

To test whether the ATRX IFF has the ability to regulate the above transcriptional pathways, we expressed a nuclear-localized C-terminal portion of ATRX that contains the helicase domain retained in the majority of ATRX IFFs identified in patients. By expressing this construct (MS2-NLS-ATRX-helicase versus MS2-NLS-empty vector control) in ATRX WT SK-N-FI cells, we observed induction of ATRX IFF-bound/IFF Up genes including *REST* and TGFβ pathway effectors *TGFBI* and *SMAD3*, as well as downregulation of REST targets by qPCR (Figure S3M). We subsequently performed a global RNA-seq analysis on these cells (Table S3). Consistent with ATRX IFF-bound/ATRX IFF Up genes as TGFβ pathway targets, ChEA analysis showed enrichment for SMAD targets in the upregulated genes (n = 75 genes) and PRC2 and REST signatures in the downregulated genes (n = 77 genes) (Figure S3N). Collectively, we demonstrate that ATRX IFF proteins occupy active promoters associated with a unique pro-oncogenic gene expression signature, including the expression of the TGFβ pathway and *REST* and concomitant downregulation of REST targets.

REST and H3K27me3 Promote Silencing of Neuronal Differentiation Genes in ATRX IFF NB

Because of the neuronal differentiation signature identified among ATRX IFF Down genes (Figures 2E–2G and 3F), coupled to robust levels of REST protein in ATRX IFF NB cells (Figure 3E), we performed REST ChIP-seq in SK-N-MM and CHLA-90. We found REST peaks primarily in promoters and gene bodies (Figure S4A), as observed at the REST target gene *CACNG2* (Figure S4B). Because genes with multiple REST peaks across promoters and gene bodies exhibit lower levels of expression than those with a single peak or those with a promoter peak alone (Rockowitz et al., 2014), we defined "REST-bound" genes as those having one or more REST peaks present within the promoter (−2 kb from the transcriptional start site [TSS]) and/or gene body (TSS to transcriptional end site [TES]) common to both ATRX IFF lines (n = 469, Table S4).

As anticipated, REST-bound genes significantly overlapped with ATRX IFF Down genes ("REST-bound/ATRX IFF Down", n = 153) (Figure 4A and Table S4). REST peaks totaled 312 at these 153 genes (Figure 4B) and we identified the REST DNA-binding motif at these peaks (Figure S4C). We further observed that REST-bound/ATRX IFF Down genes harbored higher H3K27me3, reduced H3K27ac (Figures 4C and S4B), and lower expression compared with ATRX WT NB cells (Figure 4D). These genes were also highly enriched for terminal neuronal differentiation terms annotated by GO (Figure 4E and Table S4). We also mined NB patient microarray data (Molenaar et al., 2012) and compared *ATRX* IFF NB samples for which data was available (annotated N576T and N479T) to *ATRX* WT tumors matched for age, gender, and *MYCN* status. ATRX IFF Down genes displayed lower expression in *ATRX* IFF NB patient samples and were predicted as targets of PRC2 and REST by ChEA (Figures S4D and S4E). These data further corroborated the role of REST in suppressing expression of neurogenesis genes in ATRX IFF NB.

REST has context-dependent functions in recruiting PRC1 and PRC2 to the chromatin template, which together act as co-repressors of neuronal genes (Dietrich et al., 2012; Erkek et al., 2019; Rockowitz et al., 2014). Given that REST and EZH2 co-occupancy has been associated with lower levels of expression of REST target genes versus other known co-factors (Rockowitz et al., 2014), and the fact that ATRX IFF Down genes were implicated as PRC2 targets by ChEA (Figures 3F and S4E), we analyzed H3K27me3-enriched genes and/or promoters in ATRX WT and IFF cells. Analysis of common significant peaks in SK-N-MM and CHLA-90 revealed that ATRX IFF NB had a higher number of promoters, intergenic regions, and repeats bound by H3K27me3 compared with WT ATRX NB (Figure S4F), along with a greater number of significantly called genes (Figure S4G). When examining ATRX IFF Down genes, ATRX IFF NB cells exhibited increased H3K27me3 (Figure 4F and Table S4). Moreover, the 77 downregulated genes identified in SK-N-FI cells expressing the ATRX helicase (Figure S3N) displayed increased H3K27me3 (and decreased H3K27ac) in ATRX IFF cell lines SK-N-MM and CHLA-90 (Figure S4H).

These observations were validated using H3K27me3 ChIP-seq data from two ATRX IFF NB patient tumor samples: a metastasis collected at autopsy from the retroperitoneum (SJNBL030014; IFF of exons 1 to 11) (Figures S4I–S4K) and a PDX generated from a recurrent paraspinal NB (SJNBL047443; IFF of exons 2–11). The ATRX IFF tumor specimens generally exhibited enrichment of H3K27me3 at the REST- and H3K27me3-enriched genes called in the ATRX IFF cell lines (Figure 4G and Table S4), such as the REST-bound gene *CHST8* (Figure 4H). Thus, the repression of neuronal specification genes in ATRX IFF NB appears to be reinforced by REST and H3K27me3 co-occupancy at a subset of REST target genes.

ATRX IFF NB Cell Survival Is Dependent on EZH2 and REST

We sought to determine whether ATRX IFF NB cells are dependent on a suppressed neuronal differentiation state, mediated by PRC2 and/or REST, for survival. In neural stem cells, knockdown of REST broadly upregulates neuronal gene expression, promoting differentiation (Chen et al., 1998). We assessed REST knockdown in ATRX IFF NB cells as well as the ATRX WT, *MYCN* non-amplified cell line SK-N-AS that expresses REST at detectable protein levels (Figure S5A). We observed decreased proliferation and increased apoptosis in both ATRX IFF NB cell lines with minimal sensitivity observed in the ATRX WT cell line SK-N-AS (Figures S5B–S5E). Importantly, we observed derepression of direct REST targets identified from the ChIP-seq analysis in knockdown versus control cells, supporting the role of REST as a transcriptional repressor of

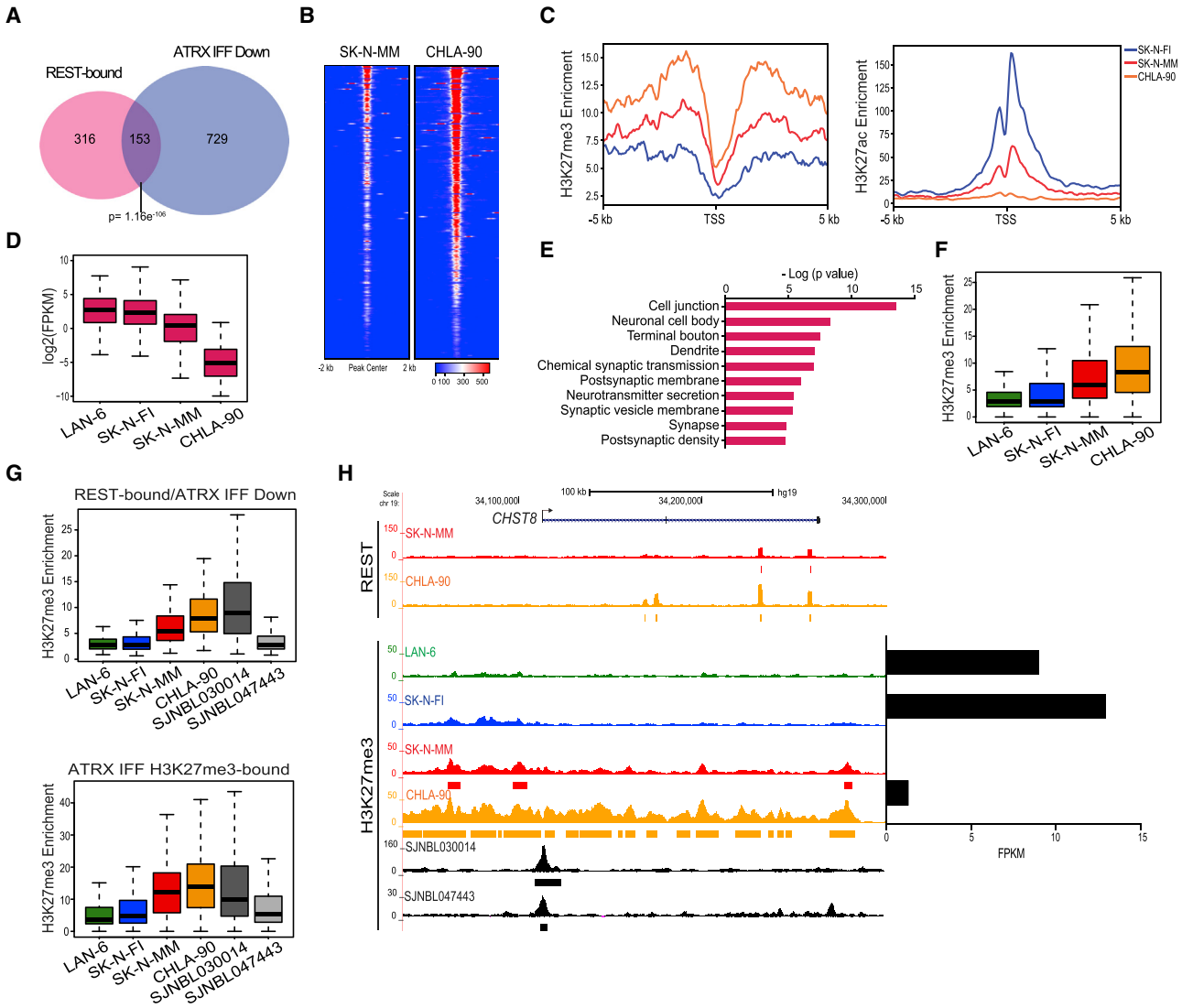

Figure 4. ATRX IFF NB Exhibits REST and H3K27me3 Co-occupancy at Repressed Neuronal Differentiation Genes

(A) Venn diagram comparing REST-bound (n = 469) and ATRX IFF Down genes (n = 826) in ATRX IFF NB cells. Statistical significance assessed using hypergeometric distribution test.

(B) Heatmap of REST peaks found in REST-bound/ATRX IFF Down genes, (±2 kb around peak center; n = 312 peaks).

(C) Metagene analysis of H3K27me3 and H3K27ac (TSS ±5 kb) enrichment at REST-bound/ATRX IFF Down genes (n = 153).

(D) Box plot of expression levels of REST-bound/ATRX IFF Down genes in NB cell lines. Box plots represent the 25th and 75th percentiles, black line indicates median, and whiskers represent extremes. Statistical significance assessed using one-way ANOVA.

(E) GO analysis of REST-bound/ATRX IFF Down genes. Enriched terms ranked by most significant p value.

(F) Box plot of H3K27me3 enrichment at ATRX IFF Down genes in NB cell lines. Box plots represent the 25th and 75th percentiles, black line indicates median, and whiskers represent extremes. Statistical significance assessed using one-way ANOVA.

(G) Box plots of H3K27me3 enrichment at ATRX IFF Down/REST-bound genes (top, n = 153) and at exclusively ATRX IFF H3K27me3-bound genes (bottom, n = 780) in ATRX IFF NB cells and NB patients/PDX. Box plots represent the 25th and 75th percentiles, black line indicates median, and whiskers represent extremes. Statistical significance assessed using one-way ANOVA.

(H) UCSC Genome Browser snapshot of REST and H3K27me3 ChIP-seq at the *CHST8* locus (y axis = reads per kilobase per million reads). Bar graph (right) indicates expression values (FPKM) for *CHST8* in corresponding cells. Significant peaks called by MACS2 (REST) and MACS2 and SICER (H3K27me3) are annotated under each profile by colored bars (FDR = 5×10^{-2} for SK-N-MM and 5×10^{-3} CHLA-90 REST peaks; 1×10^{-5} for all cell lines, 5×10^{-2} for SJNBL047443, and 1×10^{-15} for SJNBL030014 H3K27me3 peaks).

See also Figures S4 and S5; Table S4.

target neurogenesis genes (Figure S5F and Table S4). Because we also identified H3K27me3 enrichment at ATRX IFF Down genes (Figure 4F), we also performed EZH2 knockdown studies. We observed reduced proliferation and upregulation of corresponding H3K27me3-bound genes in ATRX IFF NB cells (Figures S5G–S5J and Table S4).

ATRX IFF NB Cells Are Sensitive to EZH2 Inhibitors

We next reasoned that ATRX IFF NB cells could be targeted with EZH2 inhibitors (EZH2i) to alleviate H3K27me3-mediated silencing of neuronal genes. We treated a panel of NB cells with increasing concentration of the EZH2i tazemetostat (EPZ-6438), which is under clinical development (Kim and Roberts, 2016). We confirmed that tazemetostat efficiently depleted H3K27me3, without affecting H3K9me3 (Figure 5A). With increasing dosage of tazemetostat, we found decreased proliferation, followed by increased apoptosis in ATRX IFF NB cells (at comparable concentrations used for G401, an EZH2i-sensitive *SMARCB1* [encoding SNF5]-mutant malignant rhabdoid tumor [MRT] cell line) (Knutson et al., 2013), compared with DMSO-treated cells (Figures 5B, 5C, S6A, and S6B). ATRX IFF NB cells were significantly sensitive compared with ATRX WT NB (5- to 10-fold; Figure S6A); however, we did observe mild sensitivity in some *MYCN*-amplified NB cell lines (Figures 5B and 5C), as recently reported (Chen et al., 2018). These observations were validated using two additional EZH2i, GSK126 (McCabe et al., 2012) and UNC1999 (Konze et al., 2013) (Figures S6C–S6F). Furthermore, ATRX IFF NB tumorspheres revealed a striking decrease in the percentage of live cells upon tazemetostat treatment (Figures S6G–S6I). Importantly, CHLA-90 xenografts treated with UNC1999 for 25 days displayed a significant reduction in tumor growth and volume compared with vehicle-treated tumors, reinforcing the sensitivity to EZH2i *in vivo* (Figures 5D–5F).

EZH2i Sensitivity Is Mediated by Reactivation of Neuronal Gene Signatures

To determine genes and pathways affected by EZH2i, we examined the expression profile of ATRX WT (SK-N-FI) and ATRX IFF (SK-N-MM and CHLA-90) cells treated with tazemetostat for 4 and 7 days. We utilized stringent criteria to focus on genes that were (1) exclusively upregulated in EZH2i-treated versus DMSO-treated cells, and (2) had significant H3K27me3 enrichment in untreated cells. These "EZH2i-sensitive" genes were pooled together from day 4 and day 7 in each cell line and confirmed to be on target because they were enriched for H3K27me3 and EZH2 (Figures 6A, S7A, and S7B; Table S5). Further confirming EZH2i function, SK-N-FI EZH2i-sensitive genes were also enriched for EZH2 (Figure S7B). ATRX IFF EZH2i-sensitive genes were uniquely implicated in brain development and neuronal processes by GO analysis (Figure 6B) with a common overlap of 36 genes (Figures 6C and S7A; Table S5). We also uncovered that cell-cycle and mitotic genes were significantly downregulated in ATRX IFF NB cells at day 7 (Figure S7C and Table S5), consistent with a growth arrest prior to apoptosis (Figure 5). In contrast, proliferation of ATRX WT NB cells was not reduced when treated with tazemetostat (Figure 5). Moreover, SK-N-FI cells did not show changes in expression of neurogenesis genes upon tazemetostat treatment (Figure 6C) and were associated with broad molecular and cellular GO terms (Figure S7D and Table S5). Importantly, ~10% of the total ATRX IFF EZH2i-sensitive genes were REST targets identified by our ChIP-seq (n = 42, Table S5), indicative of concordance between REST and EZH2 function.

We next validated several EZH2i-sensitive genes by qRT-PCR analysis over several time points (Figure S7E), including *NXN* (nucleoredoxin), which encodes a redox-active protein (Mu et al., 2005; Rharass et al., 2014). Derepression of *NXN* was also confirmed by immunoblot (Figure 6D). Examining UNC1999-treated CHLA-90 xenografts (Figure 5E), we confirmed upregulation of EZH2i-sensitive genes (Figure 6E), complemented by downregulation of cell-cycle genes (Figure S7F). This supports the idea that reduction of tumor growth *in vivo* was accompanied by upregulation of neurogenesis genes.

By analyzing H3K27me3 ChIP-seq data from the ATRX IFF NB tumor and PDX, we uncovered enrichment of this mark (Figure 6F) coupled to low expression of EZH2i-sensitive genes (Figure S7G and Table S5). Immunohistochemistry of the EZH2i-sensitive gene product NXN (Figure 6D) on a panel of NB tumors annotated for *ATRX* status (Cheung et al., 2012) (Table S5) revealed significantly reduced NXN staining in *ATRX* IFF and mutant NB tissues (Figure 6G). Finally, we interrogated RNA-seq data from *ATRX* WT, *MYCN*-amplified, and *ATRX*-altered patient tumors and found elevated REST expression in *ATRX* IFF/mutant patients along with reduced expression of several EZH2i-sensitive REST target genes and the EZH2i-sensitive gene *NXN* (Figure 6H and Table S5), indicating silencing of neuronal transcriptional programs in patients and, in turn, potential sensitivity to EZH2i.

REST and EZH2 Silence Common Neuronal Pathways in ATRX IFF NB

Given the neuronal signatures upregulated upon EZH2i treatment, including a subset of REST targets, and that REST was upregulated in ATRX IFF NB cells, we assessed the effect of combined REST knockdown with EZH2i (Figures S7H and S7I). First, we examined neurite outgrowth, prior to cell death (day 6), via immunostaining for neuronally expressed tubulin, βIII-tubulin (Chen et al., 2018; Rockowitz et al., 2014). We observed a higher proportion of differentiated cells in REST knockdown SK-N-MM cells, alone and in combination with EZH2i (Figure 7A). While increased neurite formation was observed in EZH2i treatment alone, it was not statistically significant compared with control, and the phenotype was most prominent in REST knockdown cells. We next examined apoptosis in ATRX IFF lines SK-N-MM and CHLA-90 under the above conditions. REST knockdown promoted apoptosis both in DMSO control and EZH2i-treated cells, with CHLA-90 knockdown cells showing almost 100% cell death in both conditions (Figure 7B). While the combination treatment did not significantly enhance cell death compared with REST knockdown alone, the effects of EZH2i in promoting cell death were somewhat premature at this time point (day 9).

Finally, we performed RNA-seq analysis on CHLA-90 REST knockdown cells prior to significant cell death and identified that genes bound by REST in CHLA-90 control cells and upregulated upon knockdown ("REST-sensitive," n = 49; Table S6) were important in neuronal processes (Figure 7C), similar to CHLA-90 EZH2i-sensitive genes (Figure 6B). Additionally, REST-sensitive genes showed significant overlap with genes upregulated upon EZH2i treatment (Figure 7D), and displayed higher H3K27me3 enrichment in both CHLA-90 and SK-N-MM compared with SK-N-FI (Figure 7E). Together with the neurite data, this suggests that the ATRX IFF NB cells are dependent on REST to maintain a suppressed neuronal differentiation state that could be perturbed by either EZH2i or REST ablation with some overlap between these two silencing pathways.

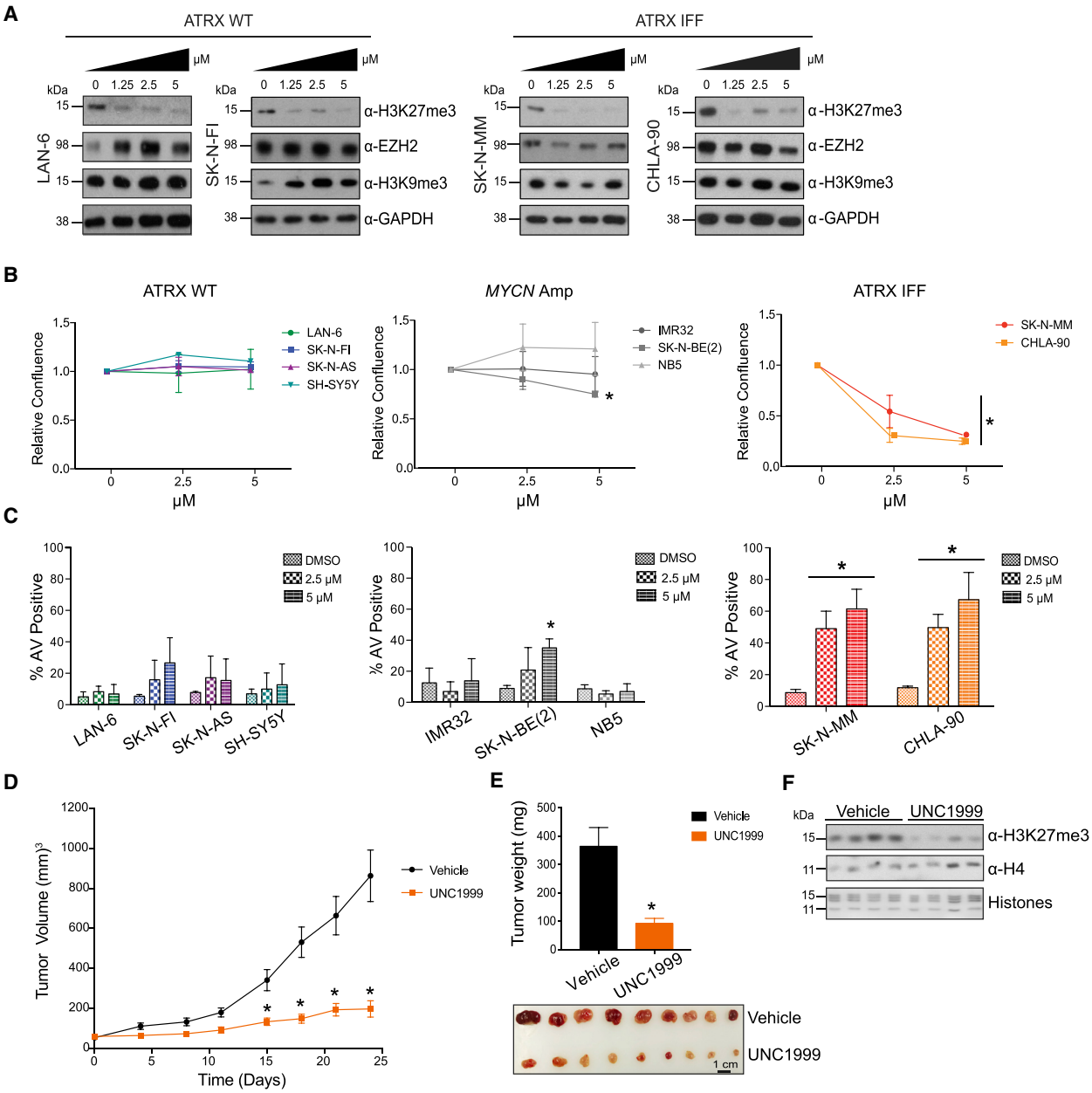

Figure 5. EZH2i Leads to Cell Death and Impaired Tumor Growth in ATRX IFF NB Cells

(A) Immunoblots for H3K27me3, EZH2, and H3K9me3 from whole-cell extracts of NB cells treated with DMSO or tazemetostat (2.5 or 5 μM) for 7 days. GAPDH used as a loading control.

(B) Cell proliferation of NB cell lines treated with DMSO or tazemetostat (2.5 or 5 μM) over 12 days. Percent confluence normalized to DMSO for each condition and plotted at day 12. Values normalized mean ± SD (n = 3). Statistical significance assessed using Student's unpaired t test with each cell line compared with DMSO, *p < 0.05.

(C) Annexin V (AV) staining of NB cells treated with DMSO or tazemetostat (2.5 or 5 μM) for 12 days. Percent AV-positive cells plotted, values are mean ± SD (n = 3). Statistical significance assessed using Student's unpaired t test with each cell line compared with DMSO, *p < 0.05.

(D) Tumor volume measurements of CHLA-90 cells subcutaneously injected into immunocompromised mice. Once tumors reached ~100 mm^3, mice were treated with vehicle or UNC1999 at 300 mg/kg of body weight for 25 days, values mean ± SEM (n = 9). Statistical significance assessed using Student's unpaired t test compared with vehicle, *p < 0.05.

(E) Tumor weight measurement from xenografts collected in (D), values mean ± SEM (n = 9), *p < 0.05. Images of excised tumors shown below.

(F) Immunoblots for H3K27me3 from acid-extracted histones derived from vehicle and UNC1999-treated xenografts. H4 immunoblot and amido black staining of histones used as loading controls.

See also Figure S6.

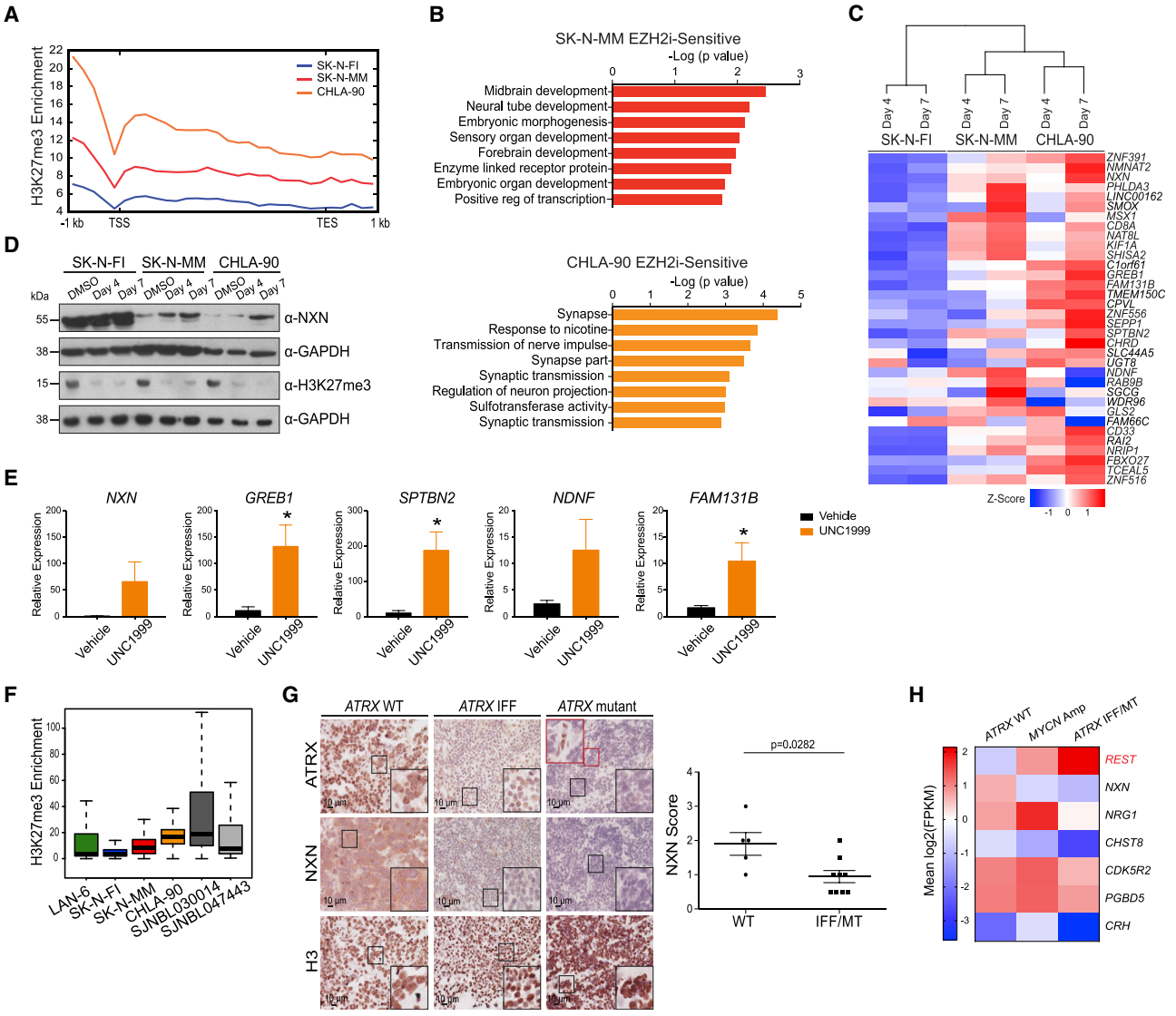

Figure 6. EZH2i Derepresses H3K27me3- and REST-Bound Neuronal Genes in ATRX IFF NB Cells

(A) Metagene analysis of H3K27me3 enrichment in indicated NB cell lines at ATRX IFF EZH2i-sensitive genes (n = 415) (TSS to TES, ±1 kb).

(B) GO analysis of genes upregulated in each ATRX IFF cell line. Enriched terms ranked by p value.

(C) Heatmap of expression levels of EZH2i-sensitive genes common to both SK-N-MM and CHLA-90 (n = 36) in all conditions.

(D) Immunoblots for NXN and H3K27me3 in whole-cell extracts from NB cell lines treated with DMSO or tazemetostat (5 μM) at days 4 and 7. GAPDH used as a loading control.

(E) qRT-PCR analysis of EZH2i-sensitive genes in vehicle- or UNC1999-treated CHLA-90 xenografts. Relative expression normalized to GAPDH, mean ± SD (n = 7). Statistical significance assessed using Student's unpaired t test with each cell line compared with control cells, *p < 0.05.

(F) Box plot of H3K27me3 enrichment at EZH2i-sensitive genes in NB cell lines, *ATRX* IFF NB tumor and PDX. Box plots represent the 25th and 75th percentiles, black line indicates median, and whiskers represent extremes. Statistical significance assessed using one-way ANOVA.

(G) Immunohistochemistry for ATRX and NXN in representative *ATRX* WT (Memorial Sloan Kettering Cancer Center [MSKCC] ID #7716), *ATRX* IFF (MSKCC ID #17473), and *ATRX* mutant (MSKCC ID #17252) NB tissue. Black insets show nuclei and the red inset shows ATRX-positive control endothelial cells in the *ATRX* mutant tumor. H3 staining used for tissue quality. Scale bars, 10 μm. NXN immunohistochemistry scoring is shown at the right; values are mean ± SEM.

(H) Expression levels of REST and ATRX IFF EZH2i-sensitive/REST targets from RNA-seq of MSKCC NB patient samples (n = 5 for each subtype).

See also Figure S7 and Table S5.

DISCUSSION

Here, we present mechanistic insight into how *ATRX* structural alterations contribute to indolent NB. ATRX IFFs generate truncated protein products retaining the ATP-dependent helicase domain that no longer bind H3K9me3, and instead are enriched at active promoters, including that of *REST* (Figure 7F). Despite losing the ADD domain, the ability of ATRX IFFs to bind chromatin is intact and is associated with increased gene expression compared with WT cells. As ATRX is a key regulator of the transcription of

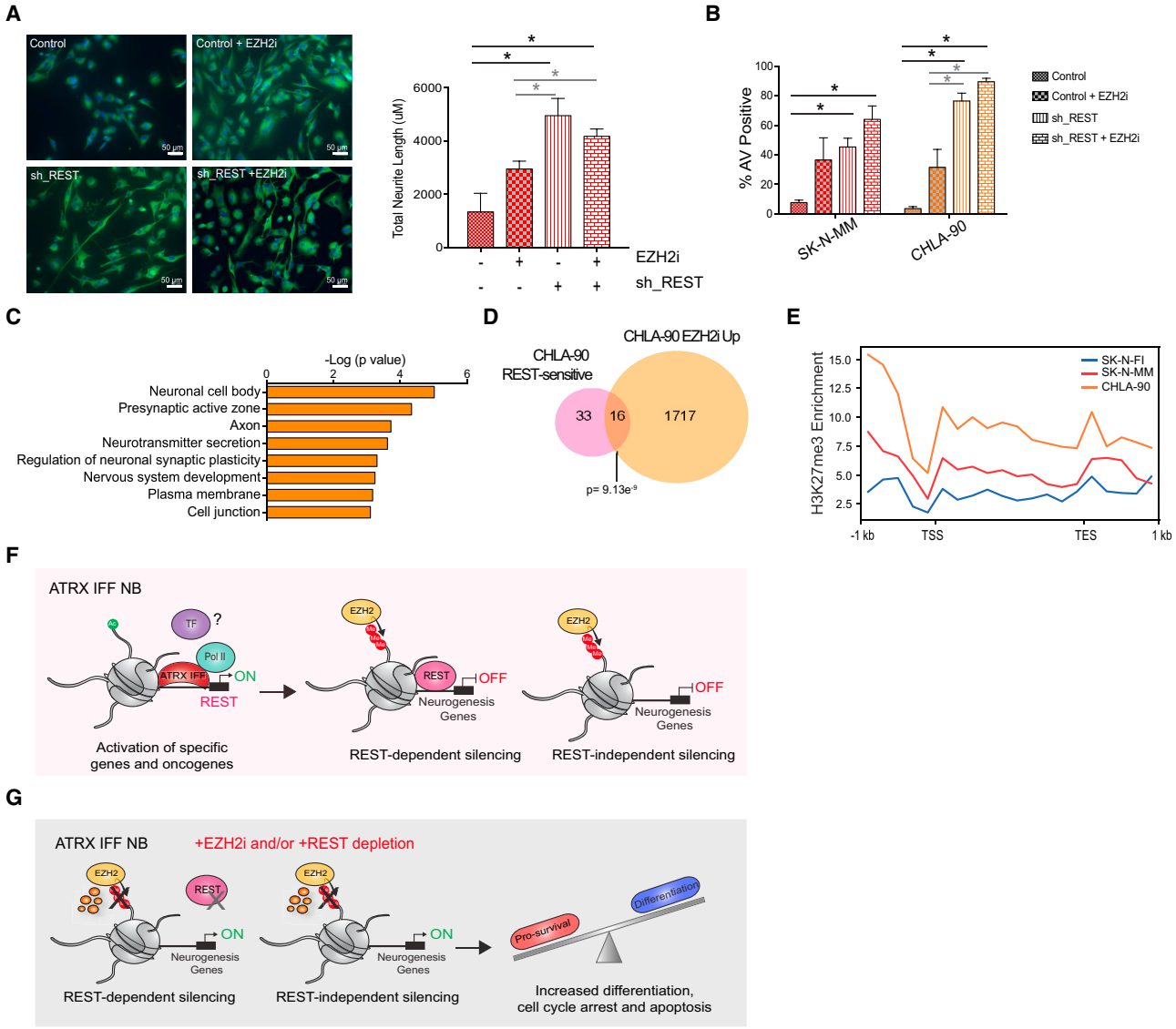

Figure 7. EZH2i or REST Ablation in ATRX IFF NB Enhances Cell Death and Neuronal Differentiation

(A) Representative immunofluorescence images for neuronal βIII-tubulin (left) and quantification of total neurite length (right) of control shRNA and REST knockdown SK-N-MM cells treated with DMSO or tazemetostat over 6 days. Values are mean ± SEM (n = 3). Scale bars, 50 μm.

(B) Annexin V (AV) staining of control and REST knockdown NB cells treated with either DMSO or tazemetostat over 9 days. Percent AV-positive cells plotted, values are mean ± SEM (n = 3). Statistical significance for (A) and (B) assessed using Student's unpaired t test with each cell line compared with control shRNA cells, *$p < 0.05$. Black bars indicate significance compared with control, and gray bars indicate significance compared with control + EZH2i. No asterisk indicates no significance.

(C) GO analysis of genes bound by REST in CHLA-90 control cells and genes upregulated in CHLA-90 REST knockdown cells at day 6 after transduction ("REST-sensitive"). Enriched terms ranked by p value.

(D) Venn diagram of CHLA-90 REST-sensitive genes and upregulated genes in CHLA-90 tazemetostat-treated cells pooled from days 4 and 7. Statistical significance assessed using hypergeometric distribution test.

(E) Metagene analysis of H3K27me3 enrichment at CHLA-90 REST-sensitive/EZH2i Up genes (n = 16) in NB cell lines (TSS to TES, ±1 kb).

(F) Model illustrating ATRX IFFs localizing to the *REST* promoter, leading to its activation and showing that REST and EZH2 cooperate to silence neurogenesis genes.

(G) Schematic demonstrating that treatment of ATRX IFF NB cells with EZH2i transcriptionally upregulates H3K27me3-enriched neurogenesis genes, a subset of which are REST bound, prompting differentiation followed by apoptosis. REST depletion has similar effects.

See also Figure S7 and Table S6.

α-globin genes (Law et al., 2010; Ratnakumar et al., 2012), we posit that ATRX IFFs can recruit transcriptional machinery to mediate *REST* reactivation and, in turn, suppress neuronal differentiation. This is further supported by our findings of a shift in ATRX IFF-containing protein complexes, indicative of additional associations to be determined in future studies.

Nuclear expression of the ATRX helicase domain in ATRX WT cells can induce gene expression changes consistent with a PRC2/REST signature of the downregulated genes. However, we found that additional ATRX WT NB cells did not tolerate ectopic expression of the ATRX helicase domain (data not shown). We suspect this to be due to the presence of a WT *ATRX* allele. As *ATRX* is X-linked and does not escape X inactivation in female somatic cells (Muers et al., 2007), there may be detrimental dosage effects of having two copies of *ATRX* or incompatibility between having a WT and an IFF copy. Thus, the pro-tumorigenic effects of ATRX IFFs in NB are likely dependent on the developmental and epigenetic landscape of the cell of origin. Future studies modeling these alterations in sympathoadrenal cell precursors will inform how ATRX IFFs perturb neural differentiation and promote neuroblastoma development.

Impaired differentiation of neuronal precursor cells is one of the characteristic features of NB tumors (Cheung and Dyer, 2013) and is presumed to drive cancer formation. We demonstrate that EZH2 inhibition induces upregulation of neuronal maturation genes bound by REST and/or H3K27me3, resulting in apoptosis of ATRX IFF NB cells (Figure 7G). Interestingly, *MYCN*-amplified NB is also sensitive to EZH2i through derepression of neuronal gene signatures; however, the genes altered upon EZH2i in *MYCN*-amplified NB were not reported to correlate with REST targets (Chen et al., 2018). Consistent with this, *REST* overexpression has been linked to stage 4 *MYCN* non-amplified NB (Liang et al., 2014). Furthermore, *ATRX* mutations and *MYCN* amplifications are mutually exclusive genomic alterations found in patients (Cheung and Dyer, 2013; Dyer et al., 2017). These genetically distinct NB tumors may develop at different stages of neural crest cell development or arise from different cells of origin, hence being sensitive to EZH2i through different gene expression programs. Thus, the use of EZH2i may be of clinical benefit to NB patients harboring either genetic alteration.

In addition to NB, high expression levels of *REST* have been detected in other cancers including glioma and medulloblastoma (Dobson et al., 2019; Taylor et al., 2012; Zhang et al., 2016). This implicates REST as a key transcription factor important in normal neurogenesis that is hijacked by cancer cells to promote proliferation/survival. We and others report co-occupancy of REST and PRC2/H3K27me3 across multiple cell types (Dietrich et al., 2012; Erkek et al., 2019; Rockowitz et al., 2014). For example, EZH2i-sensitive *SMARCB1* mutant atypical teratoid/rhabdoid tumors (ATRT) were recently reported to recruit REST to repressed SUZ12/H3K27me3-bound neuronal genes normally bound by SNF5 (Erkek et al., 2019). Further reinforcing this finding, an antagonistic relationship was observed between the EZH2-REST and SWI/SNF complex subunit BAF53b during neuronal differentiation (Lee et al., 2018). Our data suggest that REST ablation or EZH2 inhibition enhances ATRX IFF NB cell death. Therefore, the development of REST inhibitors may reinstate neuronal differentiation programs and promote proliferative arrest or cell death of REST-expressing ATRX IFF NB, alone or in combination with EZH2i.

REST protein stability was recently reported to be mediated through EZH2's methyltransferase activity in human fibroblasts (Lee et al., 2018). While we did not find that EZH2i treatment decreased REST protein levels (data not shown), our studies suggest that EZH2 and REST work cooperatively through the silencing of common REST target genes, but are not directly regulated by one another. Indeed, other studies support a more indirect association of H3K27me3 and REST targeting. RNA-mediated assembly of PRC2 and REST-containing complexes has been proposed for the long non-coding RNA *HOTAIR* with the 5′ region binding PRC2, while simultaneously tethering the LSD1/CoREST/REST complex via its 3′ region (Tsai et al., 2010). In addition to PRC recruitment, REST also interacts with various co-factors such as CoREST, LSD1, HDACs, and SIN3A to fine-tune gene expression, broadly independent of PRC2 function (McGann et al., 2014). REST may initiate gene repression by binding directly to the DNA in a sequence-specific manner. Subsequently, the PRC2 complex, which can sense transcriptional repression (Berrozpe et al., 2017; Hosogane et al., 2016; Riising et al., 2014), may be recruited to maintain the repressed state. Our data suggest cooperativity of EZH2 and REST in ATRX IFF NB at neuronal genes, but how they are co-recruited to such targets remains to be determined.

In addition to ATRX alterations, somatic mutations in other chromatin remodelers have been reported across a number of pediatric cancers. For example, *SMARCB1* mutations in MRT and ATRT are associated with altered EZH2 levels and genomic occupancy. Specifically, SWI/SNF deficiencies can contribute to increased PRC1 and PRC2 chromatin accessibility at developmental genes through destabilization of BAF complexes and subsequent chromatin eviction (Kadoch et al., 2016; Stanton et al., 2016). This promotes sensitivity to EZH2i through derepression of such genes (Helming et al., 2014; Kim and Roberts, 2016). EZH2i, such as tazemetostat, are currently in phase I/II clinical trials in patients with B cell lymphoma as well as SWI/SNF-altered solid tumors, and early results suggest therapeutic potential and limited toxicity in patients (Gulati et al., 2018; Kim and Roberts, 2016). Thus, our studies hold significance for NB and other *ATRX*-altered malignancies, such osteosarcoma, in which ATRX mutations and structural variations occur in ~29% of patients (Chen et al., 2014).

In summary, through extensive biochemical, epigenomic, and transcriptional studies, coupled to epigenetic perturbations with clinically relevant compounds *in vitro* and *in vivo*, we propose EZH2 inhibitors as a therapeutic strategy to treat ATRX IFF NB patients, for which targeted treatment options are currently lacking. We look forward to preclinical studies of EZH2i therapy in additional neuroblastoma models by the pediatric oncology research community.

STAR★METHODS

Detailed methods are provided in the online version of this paper and include the following:

- KEY RESOURCES TABLE
- LEAD CONTACT AND MATERIALS AVAILABILITY
- EXPERIMENTAL MODELS AND SUBJECT DETAILS
  - Cell Lines
  - Animals
  - Human Subjects
- METHOD DETAILS
  - RNA Extraction, cDNA Synthesis, and *ATRX* PCR Analysis

SUPPLEMENTAL INFORMATION

Supplemental Information can be found online at https://doi.org/10.1016/j.ccell.2019.09.002.

ACKNOWLEDGMENTS

The authors thank Idan Cohen, Rana Elkholi, Avi Ma'ayan, Matthew O'Connell, Ziyang Zhang, and current and former members of the E.B., R. Parsons, N. Jabado, and W.A.W. laboratories for advice, reagents, and technical support. We thank the ISMMS Genomics Core Facility, ISMMS Department of Oncological Sciences Sequencing Facility, Scientific Computing at ISMMS, Office of Research Infrastructure of the NIH to ISMMS (S10OD018522), St. Jude Hartwell Center, and St. Jude Department of Computational Biology. Bioinformatics analysis was assisted with the Bridges system (NSF award ACI-1445606) at the Pittsburgh Supercomputing Center through the Extreme Science and Engineering Discovery Environment (XSEDE) (NSF grant ACI-1548562). This work was supported by the NCI T32CA078207-11, DOD PRCRP Horizon award CA150773, and an NCI T32CA151022-07 to Z.A.Q., Instituto de Salud Carlos III (CPII16/00006 and PI14/00561, co-financed by the European Regional Development Fund) and European Commission's Framework Program 7 (Marie Curie Career Integration Grants) to M.F.S., NIH R01 CA124709 to J.M.M., NIH R01 GM122749 to J.J., Cycle for Survival and Kylie Rowand Foundation to S.S.R., and Catie Hoch Foundation grant to N.-K.V.C. This work was supported, in part, by Cancer Center Support P30 CA21765 to St. Jude Children's Research Hospital, grants to M.A.D. from the NIH (EY014867, EY018599, and CA168875), American Lebanese Syrian Associated Charities, Alex's Lemonade Stand Foundation, Tully Family Foundation, Passano Foundation, and HHMI. This work was supported by the Tisch Cancer Institute P30 CA196521, a Developmental Research Pilot Project Program (ISMMS), and St. Baldrick's Foundation to E.B.

AUTHOR CONTRIBUTIONS

Conceptualization, Z.A.Q. and E.B.; Methodology, Z.A.Q., D.V.-G., D.H., Z.S., A. Cook, C.N., L.M.G., M.Z., D.F., A.B., M.F.S., M.A.D., and E.B.; Investigation, Z.A.Q., D.V.-G., D.H., Z.S., A. Cook, C.N., A.S., L.M.G., M.Z., L.J., D.F., A. Chowdhury, X.C., D.B.F., A.B., and E.S.; Formal Analysis, Z.A.Q., D.V.-G., D.H., C.N., X.C., D.B.F., A.B., F.D., and M.F.; Validation, O.D. and E.S.; Resources, A.M., D.M., E.S., S.F., S.G., J.M.M., S.S.R., N.-K.V.C., W.A.W., J.J., M.F.S., M.A.D., and E.B.; Data Curation, L.M.G.; Writing – Original Draft, Z.A.Q. and E.B.; Writing – Review & Editing, Z.A.Q., D.V.-G., D.H., Z.S., A. Cook, C.N., W.A.W., and E.B.; Funding Acquisition, W.A.W., J.J., M.F.S., M.A.D., and E.B.; Supervision, J.J., M.F.S., M.A.D., and E.B.

DECLARATION OF INTERESTS

On behalf of Emily Bernstein, Zulekha A. Qadeer, and Dan Hasson, the Icahn School of Medicine at Mount Sinai has filed a patent application covering the subject matter of this research. N.-K.V.C. reports receiving commercial research grants from Y-mAbs Therapeutics and Abpro-Labs; holding ownership interest/equity in Y-mAbs Therapeutics, holding ownership interest/equity in Abpro-Labs, and owning stock options in Eureka Therapeutics. N.-K.V.C. is the inventor and owner of issued patents licensed by Memorial Sloan Kettering to Y-mAbs Therapeutics, Biotec Pharmacon, and Abpro-Labs. Hu3F8 and 8H9 were licensed by Memorial Sloan Kettering Cancer Center (MSKCC) to Y-mAbs Therapeutics. Both MSKCC and N.-K.V.C. have financial interest in Y-mAbs. N.-K.V.C. is an advisory board member for Abpro-Labs and Eureka Therapeutics. The other authors declare no competing interests.

Received: September 12, 2018
Revised: August 7, 2019
Accepted: September 4, 2019
Published: October 17, 2019

REFERENCES

Aldiri, I., Xu, B., Wang, L., Chen, X., Hiler, D., Griffiths, L., Valentine, M., Shirinifard, A., Thiagarajan, S., Sablauer, A., et al. (2017). The dynamic epigenetic landscape of the retina during development, reprogramming, and tumorigenesis. Neuron *94*, 550–568.e10.

Alonso, A., Bernstein, E., and Hasson, D. (2018). Histone native chromatin immunoprecipitation. Methods Mol. Biol. *1823*, 77–104.

Ballas, N., and Mandel, G. (2005). The many faces of REST oversee epigenetic programming of neuronal genes. Curr. Opin. Neurobiol. *15*, 500–506.

Berrozpe, G., Bryant, G.O., Warpinski, K., Spagna, D., Narayan, S., Shah, S., and Ptashne, M. (2017). Polycomb responds to low levels of transcription. Cell Rep. *20*, 785–793.

Boyarchuk, E., Filipescu, D., Vassias, I., Cantaloube, S., and Almouzni, G. (2014). The histone variant composition of centromeres is controlled by the pericentric heterochromatin state during the cell cycle. J. Cell Sci. *127*, 3347–3359.

Brodeur, G.M. (2003). Neuroblastoma: biological insights into a clinical enigma. Nat. Rev. Cancer *3*, 203–216.

Cardoso, C., Timsit, S., Villard, L., Khrestchatisky, M., Fontès, M., and Colleaux, L. (1998). Specific interaction between the XNP/ATR-X gene product and the SET domain of the human EZH2 protein. Hum. Mol. Genet. *7*, 679–684.

Chen, E.Y., Tan, C.M., Kou, Y., Duan, Q., Wang, Z., Meirelles, G., Clark, N.R., and Ma'ayan, A. (2013a). Enrichr: interactive and collaborative HTML5 gene list enrichment analysis tool. BMC Bioinformatics *14*, 128.

Chen, X., Stewart, E., Shelat, A.A., Qu, C., Bahrami, A., Hatley, M., Wu, G., Bradley, C., McEvoy, J., Pappo, A., et al. (2013b). Targeting oxidative stress in embryonal rhabdomyosarcoma. Cancer Cell *24*, 710–724.

Chen, L., Alexe, G., Dharia, N.V., Ross, L., Iniguez, A.B., Conway, A.S., Wang, E.J., Veschi, V., Lam, N., Qi, J., et al. (2018). CRISPR-Cas9 screen reveals a MYCN-amplified neuroblastoma dependency on EZH2. J. Clin. Invest. *128*, 446–462.

Chen, X., Bahrami, A., Pappo, A., Easton, J., Dalton, J., Hedlund, E., Ellison, D., Shurtleff, S., Wu, G., Wei, L., et al. (2014). Recurrent somatic structural variations contribute to tumorigenesis in pediatric osteosarcoma. Cell Rep. *7*, 104–112.

Chen, Z.-F., Paquette, A.J., and Anderson, D.J. (1998). NRSF/REST is required in vivo for repression of multiple neuronal target genes during embryogenesis. Nat. Genet. *20*, 136–142.

Cheung, N.-K.V., and Dyer, M.A. (2013). Neuroblastoma: developmental biology, cancer genomics and immunotherapy. Nat. Rev. Cancer *13*, 397–411.

Cheung, N.-K.V., Zhang, J., Lu, C., Parker, M., Bahrami, A., Tickoo, S.K., Heguy, A., Pappo, A.S., Federico, S., Dalton, J., et al. (2012). Association of age at diagnosis and genetic mutations in patients with neuroblastoma. JAMA *307*, 1062–1071.

Chong, J.A., Tapia-Ramirez, J., Kim, S., Toledo-Aral, J.J., Zheng, Y., Boutros, M.C., Altshuller, Y.M., Frohman, M.A., Kraner, S.D., and Mandel, G. (1995). REST: a mammalian silencer protein that restricts sodium channel gene expression to neurons. Cell *80*, 949–957.

Chung, C.-Y., Sun, Z., Mullokandov, G., Bosch, A., Qadeer, Z.A., Cihan, E., Rapp, Z., Parsons, R., Aguirre-Ghiso, J.A., Farias, E.F., et al. (2016). Cbx8 acts non-canonically with Wdr5 to promote mammary tumorigenesis. Cell Rep. *16*, 472–486.

Dhayalan, A., Tamas, R., Bock, I., Tattermusch, A., Dimitrova, E., Kudithipudi, S., Ragozin, S., and Jeltsch, A. (2011). The ATRX-ADD domain binds to H3 tail peptides and reads the combined methylation state of K4 and K9. Hum. Mol. Genet. *20*, 2195–2203.

Dietrich, N., Lerdrup, M., Landt, E., Agrawal-Singh, S., Bak, M., Tommerup, N., Rappsilber, J., Södersten, E., and Hansen, K. (2012). REST-mediated recruitment of polycomb repressor complexes in mammalian cells. PLoS Genet. *8*, e1002494.

Dignam, J.D., Lebovitz, R.M., and Roeder, R.G. (1983). Accurate transcription initiation by RNA polymerase II in a soluble extract from isolated mammalian nuclei. Nucleic Acids Res. *11*, 1475–1489.

Dobin, A., Davis, C.A., Schlesinger, F., Drenkow, J., Zaleski, C., Jha, S., Batut, P., Chaisson, M., and Gingeras, T.R. (2013). STAR: ultrafast universal RNA-seq aligner. Bioinformatics *29*, 15–21.

Dobson, T.H.W., Tao, R.-H., Swaminathan, J., Maegawa, S., Shaik, S., Bravo-Alegria, J., Sharma, A., Kennis, B., Yang, Y., Callegari, K., et al. (2019). Transcriptional repressor REST drives lineage stage-specific chromatin compaction at Ptch1 and increases AKT activation in a mouse model of medulloblastoma. Sci. Signal. *12*, eaan8680.

Law, M.J., Lower, K.M., Voon, H.P.J., Hughes, J.R., Garrick, D., Viprakasit, V., Mitson, M., De Gobbi, M., Marra, M., Morris, A., et al. (2010). ATR-X syndrome protein targets tandem repeats and influences allele-specific expression in a size-dependent manner. Cell *143*, 367–378.

Le Douarin, B., Nielsen, A.L., Garnier, J.M., Ichinose, H., Jeanmougin, F., Losson, R., and Chambon, P. (1996). A possible involvement of TIF1 alpha and TIF1 beta in the epigenetic control of transcription by nuclear receptors. EMBO J. *15*, 6701–6715.

Drané, P., Ouararhni, K., Depaux, A., Shuaib, M., and Hamiche, A. (2010). The death-associated protein DAXX is a novel histone chaperone involved in the replication-independent deposition of H3.3. Genes Dev. *24*, 1253–1265.

Dyer, M.A., Qadeer, Z.A., Valle-Garcia, D., and Bernstein, E. (2017). ATRX and DAXX: mechanisms and mutations. Cold Spring Harb. Perspect. Med. *7*, a026567.

Erkek, S., Johann, P.D., Finetti, M.A., Drosos, Y., Chou, H.-C., Zapatka, M., Sturm, D., Jones, D.T.W., Korshunov, A., Rhyzova, M., et al. (2019). Comprehensive analysis of chromatin states in atypical teratoid/rhabdoid tumor identifies diverging roles for SWI/SNF and polycomb in gene regulation. Cancer Cell *35*, 95–110.e8.

Eustermann, S., Yang, J.-C., Law, M.J., Amos, R., Chapman, L.M., Jelinska, C., Garrick, D., Clynes, D., Gibbons, R.J., Rhodes, D., et al. (2011). Combinatorial readout of histone H3 modifications specifies localization of ATRX to heterochromatin. Nat. Struct. Mol. Biol. *18*, 777–782.

Fontanals-Cirera, B., Hasson, D., Vardabasso, C., Di Micco, R., Agrawal, P., Chowdhury, A., Gantz, M., de Pablos-Aragoneses, A., Morgenstern, A., Wu, P., et al. (2017). Harnessing BET inhibitor sensitivity reveals AMIGO2 as a melanoma survival gene. Mol. Cell *68*, 731–744.e9.

Goldberg, A.D., Banaszynski, L.A., Noh, K.M., Lewis, P.W., Elsaesser, S.J., Stadler, S., Dewell, S., Law, M., Guo, X., Li, X., et al. (2010). Distinct factors control histone variant H3.3 localization at specific genomic regions. Cell *140*, 678–691.

Gulati, N., Béguelin, W., and Giulino-Roth, L. (2018). Enhancer of zeste homolog 2 (EZH2) inhibitors. Leuk. Lymphoma *59*, 1574–1585.

Hasson, D., Panchenko, T., Salimian, K.J., Salman, M.U., Sekulic, N., Alonso, A., Warburton, P.E., and Black, B.E. (2013). The octamer is the major form of CENP-A nucleosomes at human centromeres. Nat. Struct. Mol. Biol. *20*, 687–695.

Heinz, S., Benner, C., Spann, N., Bertolino, E., Lin, Y.C., Laslo, P., Cheng, J.X., Murre, C., Singh, H., and Glass, C.K. (2010). Simple combinations of lineage-determining transcription factors prime cis-regulatory elements required for macrophage and B cell identities. Mol. Cell *38*, 576–589.

Helming, K.C., Wang, X., and Roberts, C.W.M. (2014). Vulnerabilities of mutant SWI/SNF complexes in cancer. Cancer Cell *26*, 309–317.

Hosogane, M., Funayama, R., Shirota, M., and Nakayama, K. (2016). Lack of transcription triggers H3K27me3 accumulation in the gene body. Cell Rep. *16*, 696–706.

Huang, D.W., Sherman, B.T., and Lempicki, R.A. (2009). Systematic and integrative analysis of large gene lists using DAVID bioinformatics resources. Nat. Protoc. *4*, 44–57.

Iwase, S., Xiang, B., Ghosh, S., Ren, T., Lewis, P.W., Cochrane, J.C., Allis, C.D., Picketts, D.J., Patel, D.J., Li, H., et al. (2011). ATRX ADD domain links an atypical histone methylation recognition mechanism to human mental-retardation syndrome. Nat. Struct. Mol. Biol. *18*, 769–776.

Jia, S., Wu, D., Xing, C., and Meng, A. (2009). Smad2/3 activities are required for induction and patterning of the neuroectoderm in zebrafish. Dev. Biol. *333*, 273–284.

Jubierre, L., Soriano, A., Planells-Ferrer, L., París-Coderch, L., Tenbaum, S.P., Romero, O.A., Moubarak, R.S., Almazán-Moga, A., Molist, C., Roma, J., et al. (2016). BRG1/SMARCA4 is essential for neuroblastoma cell viability through modulation of cell death and survival pathways. Oncogene *35*, 5179–5190.

Kadoch, C., Williams, R.T., Calarco, J.P., Miller, E.L., Weber, C.M., Braun, S.M.G., Pulice, J.L., Chory, E.J., and Crabtree, G.R. (2016). Dynamics of BAF-Polycomb complex opposition on heterochromatin in normal and oncogenic states. Nat. Genet. *49*, 213–222.

Kapoor, A., Goldberg, M.S., Cumberland, L.K., Ratnakumar, K., Segura, M.F., Emanuel, P.O., Menendez, S., Vardabasso, C., LeRoy, G., Vidal, C.I., et al. (2010). The histone variant macroH2A suppresses melanoma progression through regulation of CDK8. Nature *468*, 1105–1109.

Kim, K.H., and Roberts, C.W.M. (2016). Targeting EZH2 in cancer. Nat. Med. *22*, 128–134.

Knutson, S.K., Warholic, N.M., Wigle, T.J., Klaus, C.R., Allain, C.J., Raimondi, A., Porter Scott, M., Chesworth, R., Moyer, M.P., Copeland, R.A., et al. (2013). Durable tumor regression in genetically altered malignant rhabdoid tumors by inhibition of methyltransferase EZH2. Proc. Natl. Acad. Sci. U S A *110*, 7922–7927.

Konze, K.D., Ma, A., Li, F., Barsyte-Lovejoy, D., Parton, T., MacNevin, C.J., Liu, F., Gao, C., Huang, X.-P., Kuznetsova, E., et al. (2013). An orally bioavailable chemical probe of the lysine methyltransferases EZH2 and EZH1. ACS Chem. Biol. *8*, 1324–1334.

Kovatcheva, M., Liao, W., Klein, M.E., Robine, N., Geiger, H., Crago, A.M., Dickson, M.A., Tap, W.D., Singer, S., and Koff, A. (2017). ATRX is a regulator of therapy induced senescence in human cells. Nat. Commun. *8*, 386.

Kumar, H.R., Zhong, X., Hoelz, D.J., Rescorla, F.J., Hickey, R.J., Malkas, L.H., and Sandoval, J.A. (2008). Three-dimensional neuroblastoma cell culture: proteomic analysis between monolayer and multicellular tumor spheroids. Pediatr. Surg. Int. *24*, 1229–1234.

Langmead, B., Trapnell, C., Pop, M., and Salzberg, S.L. (2009). Ultrafast and memory-efficient alignment of short DNA sequences to the human genome. Genome Biol. *10*, R25.

Lechner, M.S., Schultz, D.C., Negorev, D., Maul, G.G., and Rauscher, F.J. (2005). The mammalian heterochromatin protein 1 binds diverse nuclear proteins through a common motif that targets the chromoshadow domain. Biochem. Biophys. Res. Commun. *331*, 929–937.

Lee, S.W., Oh, Y.M., Lu, Y.-L., Kim, K., Yoo Correspondence, A.S., Kim, W.K., and Yoo, A.S. (2018). MicroRNAs overcome cell fate barrier by reducing EZH2-controlled REST stability during neuronal conversion of human adult fibroblasts miR-9/9* miR-124 developmental cell article microRNAs overcome cell fate barrier by reducing EZH2-controlled REST stability during neuronal conversion of human adult fibroblasts. Dev. Cell *46*, 73–84.e7.

Liang, J., Tong, P., Zhao, W., Li, Y., Zhang, L., Xia, Y., and Yu, Y. (2014). The REST gene signature predicts drug sensitivity in neuroblastoma cell lines and is significantly associated with neuroblastoma tumor stage. Int. J. Mol. Sci. *15*, 11220–11233.

Liao, Y., Smyth, G.K., and Shi, W. (2014). featureCounts: an efficient general purpose program for assigning sequence reads to genomic features. Bioinformatics *30*, 923–930.

Longair, M.H., Baker, D.A., and Armstrong, J.D. (2011). Simple Neurite Tracer: open source software for reconstruction, visualization and analysis of neuronal processes. Bioinformatics *27*, 2453–2454.

Love, M.I., Huber, W., and Anders, S. (2014). Moderated estimation of fold change and dispersion for RNA-seq data with DESeq2. Genome Biol *15*, 550.

Massagué, J. (2012). TGFβ signalling in context. Nat. Rev. Mol. Cell Biol. *13*, 616–630.

McCabe, M.T., Ott, H.M., Ganji, G., Korenchuk, S., Thompson, C., Van Aller, G.S., Liu, Y., Graves, A.P., Della Pietra, A., 3rd, Diaz, E., et al. (2012). EZH2 inhibition as a therapeutic strategy for lymphoma with EZH2-activating mutations. Nature *492*, 108–112.

McGann, J.C., Oyer, J.A., Garg, S., Yao, H., Liu, J., Feng, X., Liao, L., Yates, J.R., and Mandel, G. (2014). Polycomb- and REST-associated histone deacetylases are independent pathways toward a mature neuronal phenotype. Elife *3*, e04235.

Molenaar, J.J., Koster, J., Zwijnenburg, D.A., van Sluis, P., Valentijn, L.J., van der Ploeg, I., Hamdi, M., van Nes, J., Westerman, B.A., van Arkel, J., et al. (2012). Sequencing of neuroblastoma identifies chromothripsis and defects in neuritogenesis genes. Nature *483*, 589–593.

Mossé, Y.P., Deyell, R.J., Berthold, F., Nagakawara, A., Ambros, P.F., Monclair, T., Cohn, S.L., Pearson, A.D., London, W.B., and Matthay, K.K. (2014). Neuroblastoma in older children, adolescents and young adults: a report from the International Neuroblastoma Risk Group Project. Pediatr. Blood Cancer *61*, 627–635.

Mu, X., Fu, X., Sun, H., Beremand, P.D., Thomas, T.L., and Klein, W.H. (2005). A gene network downstream of transcription factor Math5 regulates retinal progenitor cell competence and ganglion cell fate. Dev. Biol. *280*, 467–481.

Muers, M.R., Sharpe, J.A., Garrick, D., Sloane-Stanley, J., Nolan, P.M., Hacker, T., Wood, W.G., Higgs, D.R., and Gibbons, R.J. (2007). Defining the cause of skewed X-chromosome inactivation in X-linked mental retardation by use of a mouse model. Am. J. Hum. Genet. *80*, 1138–1149.

Parker, M., Chen, X., Bahrami, A., Dalton, J., Rusch, M., Wu, G., Easton, J., Cheung, N.-K., Dyer, M., Mardis, E.R., et al. (2012). Assessing telomeric DNA content in pediatric cancers using whole-genome sequencing data. Genome Biol. *13*, R113.

Qadeer, Z.A., Harcharik, S., Valle-Garcia, D., Chen, C., Birge, M.B., Vardabasso, C., Duarte, L.F., and Bernstein, E. (2014). Decreased expression of the chromatin remodeler ATRX associates with melanoma progression. J. Invest. Dermatol. *134*, 1768–1772.

Quinlan, A.R., and Hall, I.M. (2010). BEDTools: a flexible suite of utilities for comparing genomic features. Bioinformatics *26*, 841–842.

Ramírez, F., Dündar, F., Diehl, S., Grüning, B.A., and Manke, T. (2014). deepTools: a flexible platform for exploring deep-sequencing data. Nucleic Acids Res. *42*, W187–W191.

Ratnakumar, K., and Bernstein, E. (2013). ATRX: the case of a peculiar chromatin remodeler. Epigenetics *8*, 3–9.

Ratnakumar, K., Duarte, L.F., LeRoy, G., Hasson, D., Smeets, D., Vardabasso, C., B??nisch, C., Zeng, T., Xiang, B., Zhang, D.Y., et al. (2012). ATRX-mediated chromatin association of histone variant macroH2A1 regulates α-globin expression. Genes Dev. *26*, 433–438.

Rharass, T., Lemcke, H., Lantow, M., Kuznetsov, S.A., Weiss, D.G., and Panáková, D. (2014). Ca^{2+}-mediated mitochondrial reactive oxygen species metabolism augments Wnt/β-catenin pathway activation to facilitate cell differentiation. J. Biol. Chem. *289*, 27937–27951.

Riising, E.M., Comet, I., Leblanc, B., Wu, X., Johansen, J.V., and Helin, K. (2014). Gene silencing triggers polycomb repressive complex 2 recruitment to CpG islands genome wide. Mol. Cell *55*, 347–360.

Robinson, M.D., McCarthy, D.J., and Smyth, G.K. (2010). edgeR: a Bioconductor package for differential expression analysis of digital gene expression data. Bioinformatics *26*, 139–140.

Rockowitz, S., Lien, W.-H., Pedrosa, E., Wei, G., Lin, M., Zhao, K., Lachman, H.M., Fuchs, E., and Zheng, D. (2014). Comparison of REST cistromes across human cell types reveals common and context-specific functions. PLoS Comput. Biol. *10*, e1003671.

Rouillard, A.D., Gundersen, G.W., Fernandez, N.F., Wang, Z., Monteiro, C.D., McDermott, M.G., and Ma'ayan, A. (2016). The harmonizome: a collection of processed datasets gathered to serve and mine knowledge about genes and proteins. Database (Oxford) *2016*, baw100.

Sarma, K., Cifuentes-Rojas, C., Ergun, A., Del Rosario, A., Jeon, Y., White, F., Sadreyev, R., and Lee, J.T. (2014). ATRX directs binding of PRC2 to Xist RNA and Polycomb targets. Cell *159*, 869–883.

Schoenherr, C.J., and Anderson, D.J. (1995). The neuron-restrictive silencer factor (NRSF): a coordinate repressor of multiple neuron-specific genes. Science *267*, 1360–1363.

Simovski, B., Vodák, D., Gundersen, S., Domanska, D., Azab, A., Holden, L., Holden, M., Grytten, I., Rand, K., Drabløs, F., et al. (2017). GSuite HyperBrowser: integrative analysis of dataset collections across the genome and epigenome. Gigascience *6*, 1–12.

Stanton, B.Z., Hodges, C., Calarco, J.P., Braun, S.M.G., Ku, W.L., Kadoch, C., Zhao, K., and Crabtree, G.R. (2016). Smarca4 ATPase mutations disrupt direct eviction of PRC1 from chromatin. Nat. Genet. *49*, 282–288.

Subramanian, A., Tamayo, P., Mootha, V.K., Mukherjee, S., Ebert, B.L., Gillette, M.A., Paulovich, A., Pomeroy, S.L., Golub, T.R., Lander, E.S., et al. (2005). Gene set enrichment analysis: a knowledge-based approach for interpreting genome-wide expression profiles. Proc. Natl. Acad. Sci. U S A *102*, 15545–15550.

Sun, Z., Filipescu, D., Andrade, J., Gaspar-Maia, A., Ueberheide, B., and Bernstein, E. (2018). Transcription-associated histone pruning demarcates macroH2A chromatin domains. Nat. Struct. Mol. Biol. *25*, 958–970.

Taylor, P., Fangusaro, J., Rajaram, V., Goldman, S., Helenowski, I.B., MacDonald, T., Hasselblatt, M., Riedemann, L., Laureano, A., Cooper, L., et al. (2012). REST is a novel prognostic factor and therapeutic target for medulloblastoma. Mol. Cancer Ther. *11*, 1713–1723.

Trapnell, C., Pachter, L., and Salzberg, S.L. (2009). TopHat: discovering splice junctions with RNA-Seq. Bioinformatics *25*, 1105–1111.

Trapnell, C., Roberts, A., Goff, L., Pertea, G., Kim, D., Kelley, D.R., Pimentel, H., Salzberg, S.L., Rinn, J.L., and Pachter, L. (2012). Differential gene and transcript expression analysis of RNA-seq experiments with TopHat and Cufflinks. Nat. Protoc. *7*, 562–578.

Tsai, M.-C., Manor, O., Wan, Y., Mosammaparast, N., Wang, J.K., Lan, F., Shi, Y., Segal, E., and Chang, H.Y. (2010). Long noncoding RNA as modular scaffold of histone modification complexes. Science *329*, 689–693.

Valle-García, D., Qadeer, Z.A., McHugh, D.S., Ghiraldini, F.G., Chowdhury, A.H., Hasson, D., Dyer, M.A., Recillas-Targa, F., and Bernstein, E. (2016). ATRX binds to atypical chromatin domains at the 3′ exons of zinc finger genes to preserve H3K9me3 enrichment. Epigenetics *11*, 398–414.

Vardabasso, C., Gaspar-Maia, A., Hasson, D., Pünzeler, S., Valle-Garcia, D., Straub, T., Keilhauer, E.C., Strub, T., Dong, J., Panda, T., et al. (2015). Histone variant H2A.Z.2 mediates proliferation and drug sensitivity of malignant melanoma. Mol. Cell *59*, 75–88.

Varet, H., Brillet-Guéguen, L., Coppée, J.-Y., and Dillies, M.-A. (2016). SARTools: a DESeq2- and EdgeR-based R pipeline for comprehensive differential analysis of RNA-seq data. PLoS One *11*, e0157022.

Wong, L.H. (2010). Epigenetic regulation of telomere chromatin integrity in pluripotent embryonic stem cells. Epigenomics *2*, 639–655.

Zang, C., Schones, D.E., Zeng, C., Cui, K., Zhao, K., and Peng, W. (2009). A clustering approach for identification of enriched domains from histone modification ChIP-Seq data. Bioinformatics *25*, 1952–1958.

Zhang, D., Li, Y., Wang, R., Li, Y., Shi, P., Kan, Z., and Pang, X. (2016). Inhibition of REST suppresses proliferation and migration in glioblastoma cells. Int. J. Mol. Sci. *17*, 664.

Zhang, Y., Liu, T., Meyer, C.A., Eeckhoute, J., Johnson, D.S., Bernstein, B.E., Nusbaum, C., Myers, R.M., Brown, M., Li, W., et al. (2008). Model-based analysis of ChIP-seq (MACS). Genome Biol. *9*, R137.

STAR★METHODS

KEY RESOURCES TABLE

REAGENT or RESOURCE	SOURCE	IDENTIFIER
Antibodies		
β-III-Tubulin	Abcam	Cat#ab18207; RRID: AB_444319
ATRX	Sigma	Cat#HPA001906; RRID: AB_1078249
ATRX	Abcam	Cat#ab97508; RRID: AB_10680289
BAF155	Santa Cruz	Cat#sc-9746; RRID: AB_671099
BAF47	Bethyl	Cat#A301-087A; RRID: AB_2191714
DAXX	Santa Cruz	Cat#sc-7152; RRID: AB_2088784
EZH2	Cell Signaling	Cat#5246; RRID: AB_10694683
GAPDH	Santa Cruz	Cat#sc-32233; RRID: AB_627679
GAPDH	Abcam	Cat#ab8245; RRID: AB_2107448
GFP	Roche	Cat#11814460001; RRID: AB_390913
H3	Abcam	Cat#ab1791; RRID: AB_302613
H3K27ac	Abcam	Cat#ab4729; RRID: AB_2118291
H3K27me3	Millipore	Cat#07-449; RRID: AB_310624
H3K9me3	Abcam	Cat#ab8898; RRID: AB_306848
HP1α	Millipore	Cat#05-689; RRID: AB_2290973
MEK2	BD Biosciences	Cat#610235; RRID: AB_397630
MYCN	Santa Cruz	Cat#sc-56729; RRID: AB_2266882
NR2F1	Abcam	Cat#ab41858; RRID: AB_742210
NR2F2	Abcam	Cat#ab41859; RRID: AB_742211
NXN	Sigma	Cat#HPA023566; RRID: AB_1854737
REST	Bethyl	Cat#A300-540A; RRID: AB_477960
REST	Millipore	Cat#07-579; RRID: AB_310728
SUZ12	Millipore	Cat#07-379
YAP1	Santa Cruz	Cat#sc-15407; RRID: AB_2273277
Biological Samples		
Neuroblastoma microarray	Versteeg Lab, Molenaar et al., 2012	N599T, N595T, N576T, N479T
Neuroblastoma tissue for ChIP-seq and RNA-seq	Dyer Lab, St. Jude	SJNBL030014, SJNBL047443
Neuroblastoma tissue for IHC and RNA-seq	Cheung and Roberts Lab, MSKCC	Summarized in Table S6
Chemicals, Peptides, and Recombinant Proteins		
DSG	Pierce	Cat#20593
EZH2 inhibitor EPZ-6438	Selleckchem	Cat#S7128
EZH2 inhibitor GSK126	Jian Lab, McCabe et al., 2012	N/A
EZH2 inhibitor UNC1999	Jian Lab, Konze et al., 2013	N/A
IGEPAL	Sigma	Cat#I-8896
Magna ChIP Protein A+G Magnetic beads	Millipore	Cat#16-663
Micrococcal Nuclease	Affymetrix	Cat#70196Y
Micrococcal Nuclease	NEB	Cat#M0247S
Protein A/G beads	Pierce	Cat# 88802
Superose 6 Increase 30/100 GL column	GE Healthcare	Cat# 29091597

(*Continued on next page*)

Continued

REAGENT or RESOURCE	SOURCE	IDENTIFIER
Critical Commercial Assays		
Annexin V FITC Kit	BD Biosciences	Cat#556547
BCA Protein Assay Kit	Pierce	Cat#23225
Blood and Cell Culture DNA Mini kit	Qiagen	Cat#13323
Nextera DNA Library Preparation Kit	Illumina	Cat#FC-121-1030
Platinum Taq DNA Polymerase High Fidelity	Invitrogen	Cat#11304011
Ribo-Zero Gold Kit	Illumina	Cat#MRZG12324
RNeasy Qiagen extraction kit	Qiagen	Cat#74104
TruSeq Stranded Total RNA Library Prep Kit	Illumina	Cat# 20020596
Deposited Data		
Microarray expression data of human neuroblastoma samples	Versteeg Lab, Molenaar et al., 2012	GEO: GSE16476
Raw and analyzed ChIP-seq and RNA-sequencing analysis	This paper	GEO: GSE100148
Raw and analyzed whole exome sequencing and CNV analysis	This paper	EBI: EGAS00001002507
Experimental Models: Cell Lines		
Human: CHLA-90	COG	N/A
Human: G401	ATCC	CRL-1441
Human: HEK293T	ATCC	CRL-3216
Human: IMR-32	ATCC	CCL-127
Human: LAN-6	COG	N/A
Human: NB5	St. Jude	N/A
Human: SH-SY5Y	MSKCC	N/A
Human: SK-N-AS	MSKCC	N/A
Human: SK-N-BE(2)	MSKCC	N/A
Human: SK-N-FI	MSKCC	N/A
Human: SK-N-MM	MSKCC	N/A
Human: U2OS	ATCC	HTB-96
Experimental Models: Organisms/Strains		
Mouse: female, 6 to 8 weeks old, NMRI-nude mice	Janvier Labs	N/A
Oligonucleotides		
ATRX-C-term (RT-PCR) R CATTGATTT CCCTTGGGAAGGT	Fisher Scientific	N/A
ATRX-Exon 17 (RT-PCR) R GCAATCCCA CATAAACTGAACAC	Fisher Scientific	N/A
ATRX-N-term (RT-PCR) F ATGACCGCTGAGCCCAT	Fisher Scientific	N/A
BMP7 (RT-qPCR) F TCGGCACCCATGTTCATGC	Fisher Scientific	N/A
BMP7 (RT-qPCR) R GAGGAAATGGCTATCTTGCAGG	Fisher Scientific	N/A
BSN (RT-qPCR) F TGCAAGACTTCGGACCTCAC	Fisher Scientific	N/A
BSN (RT-qPCR) R GACAGAGCCACTCCTTCACC	Fisher Scientific	N/A
CACNG2 (RT-qPCR) F GAATATTTCCTCCGGGCCGT	Fisher Scientific	N/A
CACNG2 (RT-qPCR) R GAATATTTCCTCCGGGCCGT	Fisher Scientific	N/A

(*Continued on next page*)

Continued

REAGENT or RESOURCE	SOURCE	IDENTIFIER
CHST8 (RT-qPCR) F CTGCGCCAGGTTTAAAGGTCA	Fisher Scientific	N/A
CHST8 (RT-qPCR) R CCATCAGGCCGAGATCTGAA	Fisher Scientific	N/A
FAM131B (RT-qPCR) F ACTCTGCTGTCTGAATGCCT	Fisher Scientific	N/A
FAM131B (RT-qPCR) R CTCAGTAGGGATGAGCTGGG	Fisher Scientific	N/A
GAPDH (RT-qPCR) F TTTGTCAAGCTCATTTCCTGG	Fisher Scientific	N/A
GAPDH (RT-qPCR) R TGATGGTACATGACAAGGTGC	Fisher Scientific	N/A
GREB1 (RT-qPCR) F GAGCACATGACGAAGCAGAG	Fisher Scientific	N/A
GREB1 (RT-qPCR) R AGTGTATGCGGGTTCTGGAA	Fisher Scientific	N/A
MYT1 (RT-qPCR) F GAACTACGCTTCACACCGGA	Fisher Scientific	N/A
MYT1 (RT-qPCR) R TGGAACTGGGCACTTCATCA	Fisher Scientific	N/A
NAT8L (RT-qPCR) F GGGCCTTTTGTCCTGTTAGC	Fisher Scientific	N/A
NAT8L (RT-qPCR) R AGGGTGCCGATTTCTGTACA	Fisher Scientific	N/A
NDNF (RT-qPCR) F GGACGTGGACTATTTCGCAC	Fisher Scientific	N/A
NDNF (RT-qPCR) R TTCTGGGTCCTTGAGCTGAG	Fisher Scientific	N/A
NMNAT2 (RT-qPCR) F GGAGCTGCAAGCGTTAAGGG	Fisher Scientific	N/A
NMNAT2 (RT-qPCR) R GGGGTTGCCTCTCTTTTTGTG	Fisher Scientific	N/A
NR2F1 (RT-qPCR) F CTTACACATGCCGTGCCAAC	Fisher Scientific	N/A
NR2F1 (RT-qPCR) R CACTTCTTGAGGCGGCAGTA	Fisher Scientific	N/A
NR2F2 (RT-qPCR) F TCATGGGTATCGAGAACATTTGC	Fisher Scientific	N/A
NR2F2 (RT-qPCR) R TTCAACACAAACAGCTCGCTC	Fisher Scientific	N/A
NXN (RT-qPCR) F TGGCAGACGTGTCCCTTCA	Fisher Scientific	N/A
NXN (RT-qPCR) R AGTGGTGGCGTCGAGGAATA	Fisher Scientific	N/A
PTPRN2 (RT-qPCR) F GCCTGTGTGAACGATGGAGT	Fisher Scientific	N/A
PTPRN2 (RT-qPCR) R CGACACCTCGTAGCGGTAAA	Fisher Scientific	N/A
RAI2 (RT-qPCR) F TTGGGGGAAGAGGATCACATTAAG	Fisher Scientific	N/A
RAI2 (RT-qPCR) R CTGATGCCACTTGGCCTTCC	Fisher Scientific	N/A
REST (RT-qPCR) F GCACCCAACTTTACCACCCT	Fisher Scientific	N/A

(*Continued on next page*)

Continued

REAGENT or RESOURCE	SOURCE	IDENTIFIER
REST (RT-qPCR) R GGCCATAACTGTATTCGGCCT	Fisher Scientific	N/A
RPL0 (RT-qPCR) F CAGCAAGTGGGAAGGTGTAATCC	Fisher Scientific	N/A
RPL0 (RT-qPCR) R CCCATTCTATCATCAACGGGTACAA	Fisher Scientific	N/A
RUND3CA (RT-qPCR) F AAGAAAGCGTCCTCTCGCAA	Fisher Scientific	N/A
RUND3CA (RT-qPCR) R CTGGGGCACAGGCTTTGAA	Fisher Scientific	N/A
RUNX1 (RT-qPCR) F GAACCTCGAAGACATCGGCA	Fisher Scientific	N/A
RUNX1 (RT-qPCR) R AAGGCAGTGGAGTGGTTCAG	Fisher Scientific	N/A
SHANK2 (RT-qPCR) F GGCTCAGACATGAACTCTGTGTA	Fisher Scientific	N/A
SHANK2 (RT-qPCR) R TTCTGCCTTCGCATCGTACC	Fisher Scientific	N/A
SMAD3 (RT-qPCR) F CCATCTCCTACTACGAGCTGAA	Fisher Scientific	N/A
SMAD3 (RT-qPCR) R CACTGCTGCATTCCTGTTGAC	Fisher Scientific	N/A
SPTBN2 (RT-qPCR) F GAGCTGGCTGCCAACAAAGA	Fisher Scientific	N/A
SPTBN2 (RT-qPCR) R GTCTCTCAGCTTCTCCGACAC	Fisher Scientific	N/A
SYT14 (RT-qPCR) F GACTCAGCGCGTCCTCC	Fisher Scientific	N/A
SYT14 (RT-qPCR) R CTCTCCACCTTCAATCGCCA	Fisher Scientific	N/A
TGFBI (RT-qPCR) F CACTCTCAAACCTTTACGAGACC	Fisher Scientific	N/A
TGFBI (RT-qPCR) R CGTTGCTAGGGGCGAAGATG	Fisher Scientific	N/A
YAP1 (RT-qPCR) F GAACTCGGCTTCAGGTCCTC	Fisher Scientific	N/A
YAP1 (RT-qPCR) R TCATGGCAAAACGAGGGTCA	Fisher Scientific	N/A
Telomere (qPCR) F CGGTTTGTTTGGGTTTGGGTTTG GGTTTGGGTTTGGGTT	Fisher Scientific	N/A
Telomere (qPCR) R GGCTTGCCTTACCCTTACCCTTA CCCTTACCCTTACCC	Fisher Scientific	N/A
Recombinant DNA		
GFP-human-ATRX-C (1670-2942)	Ratnakumar et al., 2012	N/A
GFP-human-ATRX-mid (800-1670)	Ratnakumar et al., 2012	N/A
GFP-human-ATRX-N (1-841)	Ratnakumar et al., 2012	N/A
MS2-NLS	Addgene	Cat#61426
MS2-NLS-ATRX-helicase	This paper	
pLKO.1-human-sh_EZH2	Sigma-Aldrich	TRCN0000353069
pLKO.1-human-sh_NSC	Sigma-Aldrich	SHC016
pLKO.1-human-sh_REST	Sigma-Aldrich	TRCN0000014787

(*Continued on next page*)

Continued

REAGENT or RESOURCE	SOURCE	IDENTIFIER
pLKO.1-human-sh_ATRX #1	Sigma-Aldrich	TRCN0000013588
pLKO.1-human-sh_ATRX #2	Sigma-Aldrich	TRCN0000013589
Software and Algorithms		
BedTools	Quinlan and Hall, 2010	https://bedtools.readthedocs.io/en/latest/
Bowtie2	Langmead et al., 2009	http://bowtie-bio.sourceforge.net/bowtie2/index.shtml
Cuffdiff	Trapnell et al., 2012	http://cole-trapnell-lab.github.io/cufflinks/cuffdiff/
Cufflinks	Trapnell et al., 2012	http://cole-trapnell-lab.github.io/cufflinks/
deepTools	Ramírez et al., 2014	https://deeptools.readthedocs.io/en/develop/
DESeq2	Love et al., 2014	https://bioconductor.org/packages/release/bioc/html/DESeq2.html
edgeR	Robinson et al., 2010	https://bioconductor.org/packages/release/bioc/html/edgeR.html
Enrichr	Chen et al., 2013a	http://amp.pharm.mssm.edu/Enrichr/
featureCounts	Liao et al., 2014	http://subread.sourceforge.net/
FlowJo	N/A	https://www.flowjo.com/
GO	Huang et al., 2009	https://david.ncifcrf.gov/
GSEA	Subramanian et al., 2005	http://www.broadinstitute.org/gsea/index.jsp
GSuite Hyperbrowser v2.0	Simovski et al., 2017	https://hyperbrowser.uio.no/hb/#!mode=basic
HOMER	Heinz et al., 2010	http://homer.ucsd.edu/homer/index.html
MACS2	Zhang et al., 2008	http://liulab.dfci.harvard.edu/MACS/
RStudio	N/A	https://www.rstudio.com/
SICER	Zang et al. 2009	https://home.gwu.edu/~wpeng/Software.htm
Simple Neurite Tracer	Longair et al., 2011	https://imagej.net/Simple_Neurite_Tracer
STAR	Dobin et al., 2013	N/A
TopHat	Trapnell et al., 2009	https://ccb.jhu.edu/software/tophat/index.shtml

LEAD CONTACT AND MATERIALS AVAILABILITY

Further information and requests for resources and reagents should be directed to and will be fulfilled by the Lead Contact, Emily Bernstein (emily.bernstein@mssm.edu).

EXPERIMENTAL MODELS AND SUBJECT DETAILS

Cell Lines

LAN-6 (Male), IMR-32 (Male), NB5 (Female), and SK-N-MM (Female) were cultured in RPMI with 10% FBS and 1x penicillin/streptomycin. HEK293T (female), SK-N-FI (Male), SK-N-AS (Female), G401 (Male), and U2OS (Female) were cultured in DMEM with 10% FBS and 1x penicillin/streptomycin. CHLA-90 (Male) was cultured with DMEM with 20% FBS and 1x penicillin/streptomycin. SH-SY5Y (Female) and SK-N-BE(2) (Male) were cultured with DMEM/F12 with 10% FBS and 1x penicillin/streptomycin. Cell authentication was confirmed with STR profiling.

Animals

6-8-week-old female NMRI-nude mice (Janvier Labs) were used for *in vivo* studies. For animal studies, all procedures were approved by the ethical committee of Vall d'Hebron Research Institute (protocol number 57.13).

Human Subjects

Use of human tissues for this study was approved by the institutional review boards of MSKCC (IRB 16-184), University Hospital Vall d'Hebron (Spanish Biobank National Register, Section Collections, Ref. C.0002311) and St. Jude (XPD09-234 MAST- Molecular Analysis of Solid Tumors). Patient samples from MSKCC and St. Jude were collected as outlined (Chen et al., 2014; Cheung et al., 2012). Primary tumor tissue samples from Vall d'Hebron Hospital (Barcelona, Spain) were obtained immediately after surgery and snap frozen in liquid nitrogen. Tumors were examined by a pathologist to confirm NB diagnosis, presence of $\geq$80% of tumor tissue, and histopathological classification. All patients provided written informed consent. Sample size and sample ID information of MSKCC cohort analyzed is summarized in Table S5.

METHOD DETAILS

RNA Extraction, cDNA Synthesis, and *ATRX* PCR Analysis

RNA was extracted using the QIAGEN RNeasy Mini Kit. 1 μg of total RNA was used to synthesize complementary DNA (cDNA) with First-strand cDNA Synthesis Kit (OriGene). RT-qPCR and gene expression analysis was carried out as described (Vardabasso et al., 2015). PCR amplification was performed using Polymerase Taq (Invitrogen) and amplicons were analyzed on a 1% ethidium-bromide stained agarose gel. Primers for ATRX PCR fragments in Figure S1C were previously described (Qadeer et al., 2014). Other primer sequences used are listed in the Key Resources Table.

Telomere PCR

qPCR was done as described previously (Cheung et al., 2012). Briefly 10 ng of DNA was subject to qPCR using 2 sets of primers in separate reactions, 1 to amplify telomeric sequence and 1 to amplify a housekeeping gene, RPL0. Delta Ct was calculated for every cell line by subtracting Ct values of the telomere reactions from Ct value of RPL0.

Whole-Exome Sequencing and Copy Number Variation Analysis

DNA was extracted from cells using Qiagen Blood and Cell Culture DNA Mini kit. DNA was processed using the Nextera Rapid Capture kit (Illumina, San Diego, CA), with pre-capture pooling. Pooled libraries were quantified using the Quant-iT PicoGreen dsDNA assay (Life Technologies), Kapa Library Quantification kit (Kapa Biosystems, Wilmington, Massachusetts) or low pass sequencing on a MiSeq nano kit (Illumina, San Diego, CA). One hundred cycle paired end sequencing was performed on an Illumina HiSeq 2500 or 4000. For CNVs, custom capture and clonal analysis was performed as described (Chen et al., 2013b).

Chromatin Fractionation, Acid Extraction of Histones and Immunoblots

Chromatin fractionation and acid extraction of histones were performed as described (Vardabasso et al., 2015). Extracts were resuspended directly in 2X Laemmli loading buffer with subsequent boiling. Membranes were incubated with indicated antibodies listed in the Key Resources Table.

Whole-Cell Extract Preparation and Immunoblots

Whole cell extract was prepared as described (Sun et al., 2018) by sonication in RIPA buffer supplemented with 0.125 unit/ul Benzonase (Millipore). Membranes were incubated with indicated antibodies listed in the Key Resources Table.

ATRX C-Terminal Antibody Validation

GFP tagged ATRX N terminal fragment (N-term, 1-841), middle fragment (middle, 800-1670) and C terminal fragment (C-term, 1670-2492) (Ratnakumar et al., 2012) were transiently expressed in HEK293T cells using jetPRIME (Polyplus). Whole-cell extract was prepared 40 hours post-transfection by sonication in Buffer G 150 (50 mM Tris, pH 7.5, 150 mM NaCl, 0.5% NP-40) with 0.125 unit/ul Benzonase (Millipore). Lysates were blotted with anti-GFP antibody (Roche 1181460001) that recognizes all three GFP-tagged fragments, and anti-ATRX antibody (Abcam ab97580) that was raised against the C-terminus of ATRX (aa 2211-2413).

Immunofluorescence

Immunofluorescence was performed as previously described (Boyarchuk et al., 2014). Cells grown on coverslips were incubated with anti-ATRX (Sigma HPA001906), anti-HP1α (Millipore 05-689), and anti-H3K9me3 (Abcam ab8898) antibodies and secondary antibodies conjugated with Alexa Fluor 488 and 594 (Molecular Probes). Nuclei were counterstained with Hoechst 33342 and slides were mounted in ProLong Gold (Molecular Probes). Images were acquired on a Zeiss LSM780 confocal microscope using a 40X objective, 2X internal magnification and an optimum voxel size determined by the Zeiss Zen software. Maximum intensity projections of Z-stacks are shown.

Cellular Fractionation

Cellular fractionation was performed essentially as previously described (Dignam et al., 1983). Buffers were supplemented with 0.5 mM dithiothreitol, 0.5 mM phenylmethyl sulfonyl fluoride and 1× protease inhibitor cocktail. Cells were resuspended and swollen in hypotonic buffer (10 mM HEPES, pH 7.9, 10 mM KCl, 1.5 mM $MgCl_2$) and nuclei were isolated by trituration with a 27G needle. Nuclei were pelleted and supernatant taken as the cytoplasmic fraction. Nuclei were resuspended in low salt buffer (20 mM HEPES, pH 7.9, 1.5 mM $MgCl_2$, 0.2 mM EDTA, 25% glycerol) and NaCl concentration was adjusted to 150 mM, 420 mM or 600 mM by adding 5 M NaCl drop-by-drop while vortexing. Nuclei were extracted for 30 min at 4°C with tumbling. Chromatin was pelleted and supernatant was taken as soluble nuclear extract at varying salt concentrations. Chromatin pellet was solubilized in Laemmli buffer by sonication.

Size Exclusion Chromatography

Nuclear extracts were prepared and separated on a size-exclusion column as previously described (Chung et al., 2016). NB cells were harvested with trypsin, washed with PBS, and pelleted to approximately 3-3.5 mL. Pellets were washed in 5-packed cell volumes (pcv) hypotonic buffer (10 mM HEPES, pH 7.9, 10 mM KCl, 1.5 mM $MgCl_2$, 0.5mM dithiothreitol). Cells were resuspended

in 3 pcv hypotonic buffer and allowed to swell for 10 minutes. Nuclei were isolated by dounce homogenization with 10 strokes of a type B/loose pestle. Pelleted nuclei were resuspended in 1 pcv 420 mM salt buffer (20 mM HEPES, pH 7.9, 420 mM NaCl 1.5 mM $MgCl_2$, 0.2 mM EDTA, 25% (v/v) glycerol, 0.5 mM dithiothreitol) and were extracted for 30 minutes with tumbling. Extract was clarified with centrifugation and resulting soluble extract was concentrated using centrifugal filters (Amicon 10000MWCO). The Superose 6 Increase 30/100 GL column (GE Healthcare) controlled by the AKTA Pure Chromatography System (GE Healthcare) was equilibrated with 2 column volumes of running buffer (20 mM Tris pH 7.5 150 mM NaCl 2 mM EDTA 10% glycerol and 1mM dithiothreitol), followed by injection of 500 μL of freshly prepared extract. Samples were eluted at 0.3 mL/min and 0.5 mL fractions were collected. Equal amounts of every second fraction starting at 0.35 column volume were immunoblotted with antibodies against ATRX (Abcam ab97508), DAXX (Santa Cruz sc-7152), EZH2 (Cell Signaling 5246), BAF155 (Santa Cruz sc-9746), and BAF47 (Bethyl A301-087A). Estimated sizes per column volume were determined using protein standards (Sigma-Aldrich MWGF1000) and the same running buffer and AKTA settings.

MNase Immunoprecipitation

MNase IP was performed as previously described (Sun et al., 2018) with the following modifications. Cells were lysed in PBS with 0.1% Triton X-100 for nuclei isolation and 1 ul MNase (NEB) per 10 million cells were used for chromatin digestion. Nuclei were pelleted and the mononucleosome-enriched supernatant was quantified spectroscopically (Absorbance A_{260}). Equal amount of chromatin from each cell line was used for IP. IP was performed with antibodies followed by incubation with protein A/G beads (Pierce). IP was washed three times with Buffer G 150 with 0.01% NP-40. Membranes were incubated with antibodies against ATRX (Abcam ab97508), DAXX (Santa Cruz sc-7152), EZH2 (Cell Signaling 5246), and SUZ12 (Millipore 07-379).

ChIP-seq

Native ChIP-seq was performed in all NB cell lines as described (Alonso et al., 2018; Chung et al., 2016; Hasson et al., 2013) using antibodies against H3K27me3 (Millipore 07-449) and H3K9me3 (Abcam ab8898). Cross-linked ChIP-seq was performed as previously described (Fontanals-Cirera et al., 2017) with antibodies against ATRX (Abcam ab97508), REST (Millipore 07-579), EZH2 (Cell Signaling 5246), and H3K27ac (Abcam ab4729). Cells for ATRX and REST ChIP were double cross-linked with disuccinimidyl glutarate (DSG) followed by 1% formaldehyde. Input DNA was used to control for background. Libraries were sequenced on Illumina Hi-Seq2500 or NextSeq500 (50-75bp single-end reads). Cross-linked ChIP-seq for H3K27me3 was performed for the NB IFF tumor samples by Active Motif as previously described (Aldiri et al., 2017).

ChIP-seq Analysis

Analysis was performed as previously described (Fontanals-Cirera et al., 2017; Valle-García et al., 2016). Briefly, sequenced reads were aligned to the human hg19 (GRCh37/hg19) assembly using Bowtie2 (Langmead et al., 2009). Coverage tracks were generated from BAM files using deepTools (v2.4.1). Peak calling was performed with MACS2 (Zhang et al., 2008) and/or SICER (Zang et al., 2009) to generate a final list of peaks (FDR < $5x10^{-2}$ for SK-N-FI ATRX, $5x10^{-3}$ for SK-N-MM ATRX, $5x10^{-4}$ for CHLA-90 ATRX; $5x10^{-2}$ for H3K9me3 for all cell lines; $5x10^{-2}$ for SK-N-MM REST and $5x10^{-3}$ for CHLA-90 REST; $1x10^{-5}$ for H3K27ac for all cell lines; $1x10^{-5}$ for H3K27me3 for all cell lines, $1x10^{-15}$ for SJNBL030014 H3K27me3, and $5x10^{-2}$ for SJNBL047443 H3K27me3). Summary of aligned reads and called peaks are in Table S7.

Genomic Distribution Analyses

Promoters (-2 kb to TSS for REST; -2 kb to +2 kb relative to the TSS for all other ChIPs) and gene bodies (TSS to TES) were defined according to human hg19 (GRCh37/hg19) gene annotation of Ensembl. Enhancers were classified by levels of H3K27ac; overlap of ATRX and H3K9me3 enriched regions were considered by intersecting the overlapping significant peaks from those two ChIPs; all other regions defined as other. Genes with overlapping one or more peak at the promoter, gene body or both were considered bound. Analysis of bound genes for each corresponding ChIP in its respective cell line was performed using bedTools (Quinlan and Hall, 2010), deepTools (Ramírez et al., 2014), and in-house scripts. H3K27me3 WT-bound genes was defined as having one or more H3K27me3 peak at that promoter and/or gene body in both ATRX WT cell lines and absent in either of the ATRX IFF cell lines. The reverse definition was used for H3K27me3 ATRX IFF-bound genes as well as for ATRX and REST. Gene body- and promoter-bound genes were merged to generate a final list. Observed/expected forbes coefficient ratios were calculated using the GSuite Hyperbrowser v2.0 (Simovski et al., 2017), with 10,000 montecarlo samplings to calculate the random expected distribution.

Metagene, Heatmaps and Boxplots

Analysis was performed as previously described (Fontanals-Cirera et al., 2017; Valle-García et al., 2016). Metagene, heatmaps and boxplots of enrichment at promoters or genes were generated with deepTools and R (v3.3.3). Heatmaps and boxplots for RNA-seq data were generated using R (v3.3.3).

RNA-seq

For cell lines, RNA was prepared using TRIzol (Life Technologies) and extracted using RNeasy Plus Mini kit (Qiagen #74134). For tissue, samples were first homogenized at 17000 rpm for 30 seconds with a tissue homogenizer (Polytron, PT10-35GT). Libraries were prepared from 250- 500 ng total RNA with the TruSeq Stranded Total RNA Library Prep Kit according to the manufacturer's directions

(Illumina, San Diego, Ca.) For SK-N-FI MS2-NLS-ATRX-helicase and CHLA-90 REST knockdown experiments, poly-A RNA was isolated using NEXTFLEX® Poly(A) Beads and libraries prepared with the NEXTFLEX® Rapid Directional RNA-Seq Library Prep Kit (PerkinElmer). Single-end or paired-end 75-100 bp sequencing was performed on HiSeq 2000, HiSeq 2500, or NextSeq500 according to the manufacturer's protocol (Illumina). RNA-seq in Tazemetostat treated cells SK-N-FI, SK-N-MM and CHLA-90 was performed as described (Chung et al., 2016; Fontanals-Cirera et al., 2017).

RNA-seq Analysis

Analysis for NB cell lines and Tazemetostat treated cells was conducted as previously described (Chung et al., 2016; Fontanals-Cirera et al., 2017). In brief, sequencing reads were mapped to the reference genome (GRCh37/hg19) by TopHat 1.4.0 (Trapnell et al., 2009). Transcripts were assembled by Cufflinks program 1.3.0 (Trapnell et al., 2012) with quartile normalization and bias correction functions. Differential expression analysis was performed by Cuffdiff (Trapnell et al., 2012). For NB cell lines, fragment per kilobase of transcript per million (FPKM) values for each cell line were log2 transformed. ATRX IFF and ATRX WT values were averaged and differentially expressed genes were identified with a log2 fold-change >3 for ATRX IFF Up and <-3 for ATRX IFF Down (8-fold difference). For NB patient data (St. Jude and MSKCC), reads were mapped and assigned to the genes from Ensembl's GRCh37/hg19 annotation using STAR (Dobin et al., 2013) and the featureCounts (Liao et al., 2014) program from the Rsubread package (v1.20.6) in R. The FPKM was calculated using the fpkm function from the edgeR package (v 3.12.1). Genes with a count per million < 1 were marked as not transcribed. For Tazemetostat treated cells, differentially expressed genes were analyzed with a log2 fold-change >2 compared to DMSO for each cell line on a log2 scale. For SK-N-FI MS2-NLS-ATRX-helicase and CHLA-90 REST knockdown experiments, reads were mapped and assigned using STAR and featureCounts. The log2 fold change was calculated with DESeq2 (Varet et al., 2016) and differentially expressed genes were identified with a log2 fold-change >0.8-1 and p value<0.05. Gene Set Enrichment Analysis (GSEA, Broad Institute, http://www.broadinstitute.org/gsea/index.jsp) was performed using gene sets in the MSigDB database or published gene sets as indicated (Subramanian et al., 2005). Gene Ontology (GO) was conducted using DAVID (Huang et al., 2009). ChEA analysis was performed using Enrichr (Chen et al., 2013a). REST target identification was performed using ChEA and Harmonizome (Rouillard et al., 2016).

Trans-well Migration Assay

Assays were performed as previously described (Kapoor et al., 2010). NB cells that migrated after 20 hours were fixed in 10% methanol/acetic acid solution, stained with 1% crystal violet. The number of migrated cells in 4 randomly selected microscopic fields (20x magnification) per membrane was counted.

Telomere FISH

Interphase fluorescence *in situ* hybridization (FISH) was performed on 4 μm sections of formalin-fixed, paraffin-embedded (FFPE) tissue blocks of NB tumors, as previously described (Parker et al., 2012), using Cy3-labeled TelG probe (PNAbio). Nuclei were counterstained with DAPI (200 ng/ml; Vector Labs). ALT-positivity was determined by the presence of large ultra-bright intranuclear telomeric foci.

Constructs, Lentiviral Production, and Stable Cell Infection

Lenti-MS2-P65-HSF1 (Addgene) was modified such that P65 and HSF1 coding sequences were removed. ATRX cDNA corresponding to the amino acids A1282 to M2492 (including ATRX helicase domain) was cloned into the Lenti-MS2 plasmid in-frame with the MS2 coding sequence and the SV40 nuclear localization sequence. pLKO.1-based shRNAs (TRC Lentiviral shRNA, Open Biosystems) were used for ATRX (TRCN0000013588 and TRCN0000013589), EZH2 (TRCN0000353069) and REST (TRCN0000014787) knockdown experiments. For lentiviral vectors production HEK293T cells were co-transfected with 12 μg of lentiviral expression constructs, 8 μg of psPAX2 and 4 μg pMD2.G vectors using Lipofectamine 2000 (Invitrogen) or *Trans*IT-Lenti Transfection Reagent (Mirus), following manufacturer's recommendations. At 48 and 72 hours post transfection, supernatants were collected and filtered (0.45 μm). NB cells were infected lentiviral supernatant supplemented with polybrene at a final concentration of 5 μg/mL.

EZH2 Inhibitor Treatments

NB cell lines and G401 cells were treated with EZH2 inhibitors Tazemetostat, GSK126, and UNC1999 at indicated concentrations. Media was changed every 3 days with fresh inhibitor for up to 12 days.

Cell Proliferation and Flow Cytometry

Equal number of NB cells were plated into 6-, 12-, or 24-well plates and treated with EZH2i as indicated. Cells were imaged and quantified using the Incucyte™ Live-Cell Imaging System every 3 days during treatment. For apoptosis analysis, EZH2i treated cells were collected as described above at day 12 of treatment, and labeled with FITC-Annexin V in binding buffer (BD Biosciences). All FACS analyses were performed using BD LSRFortessa and FlowJo 6.7 softwares.

Tumorsphere Formation Assay

NB multicellular tumorspheres were generated as previously described (Jubierre et al., 2016; Kumar et al., 2008). Briefly, equal number of cells was seeded in non-adherent 6-well plates (Corning) in serum-free neurobasal medium (Invitrogen), supplemented with

B27 (Invitrogen), 2 mM L-glutamine, 20 ng/ml EGF, 20 ng/ml FGF2, 20 U/ml penicillin and 20 mg/ml streptomycin. The next day, spheres were treated with EZH2 inhibitors as indicated and media was changed every 3 days. At day 12 post-treatment, spheres were dissociated with trypsin, stained with trypan blue and viable cells quantified.

In Vivo Mouse Xenograft Assay

UNC1999 powder (verified by HPLC and mass spectrometry) was slowly dissolved, incorporated to vehicle (0.5% of sodium carboxymethylcellulose [NaCMC] and 0.1% of Tween-80 in sterile water), and vortexed to achieve a homogenous suspension at a 17.5 mg/ml concentration. CHLA-90 cells (5×10^6cells/mouse) were injected in the flank of 6-8-week-old female NMRI-nude mice (n=10/group) in 300 μl of phosphate-buffered saline and Matrigel (1:1). When the tumors reach ~100mm^3, mice were randomized into two groups and vehicle or UNC1999 was administered by oral gavage. Mouse weight was monitored daily and tumor growth was measured every 2-3 days using an electronic caliper.

Neurite Outgrowth Assay

Control and REST knockdown cells were grown on coverslips and treated with EZH2i for 6 days. Cells were next fixed with 4% PFA, blocked with 5% BSA, and then probed with anti-β-III Tubulin (Abcam ab18207) overnight at 4°C. Cells were washed with PBS and incubated with secondary antibody conjugated to Alexa Fluor 488. Nuclei were counterstained and coverslips mounted onto slides with DAPI Flouromount-G (Electron Microscopy Sciences). Images were acquired on a Zeiss AxioImager M1 using the 20X objective. Within each image, neurite lengths were traced from the neuronal nuclei of each cell and quantified with the ImageJ Simple Neurite Tracer (Longair et al., 2011).

Immunohistochemistry

Immunohistochemistry was performed as previously described (Cheung et al., 2012; Qadeer et al., 2014). For ATRX IHC, endothelial cells were used as positive internal controls. Slides were incubated with antibodies listed in the Key Resources Table. The number of positive cells in each slide was scored on 3-point scale (0=<10%; 1=10-30%; 2=30-60%; 3=60-100%) by two independent pathologists in a blinded fashion.

QUANTIFICATION AND STATISTICAL ANALYSIS

Statistical Methodologies

Statistical analysis was performed using unpaired Student's t-test unless otherwise indicated. P values are represented as * and denotes p value<0.05. Statistical tests performed as part of the whole exome, DNA methylation, RNA-seq and ChIP-seq analyses are detailed in relevant sections above. Statistical analysis for box plots was performed using one-way ANOVA. Box plot statistics summarized in Tables S2, S4, and S5.

DATA AND CODE AVAILABILITY

Data Deposition

Whole-exome sequencing and CNV data for this study was deposited in European Bioinformatics Institute (EBI) European Genome-phenome Archive (EGA). The accession number for the data is EBI: EGAS00001002507. All RNA-sequencing and ChIP-sequencing data that supports this study was deposited in the National Center for Biotechnology Information (NCBI) Gene Expression Omnibus (GEO). The accession number for the RNA-sequencing and ChIP-sequencing data is GEO: GSE100148.